nature electronics

Supplementary information

https://doi.org/10.1038/s41928-026-01688-z

Soft-matter multistate ionic neuromorphic processing based on cascaded-heterointerface ion traps

In the format provided by the authors and unedited

Table of contents

Section 1: Supplementary Information Methods

Ionic rectification characteristics

The ionic rectification measurements were performed using the Keithley 2636B SourceMeter (Keithley Instruments, Cleveland, OH) and a pair of Ag/AgCl electrodes. The *I-V* characteristics, absolute transient current responses, built-in ionic potentials relaxation characteristics, and long-term rectification stability were measured using cylindrical GITs with fixed dimensions (250 μm diameter, 1.5 mm length). In the *I-V* characteristic measurements, periodic voltage sweeps of ±12 mV and ±18 mV were applied at scan rates of 1, 2, 5, and 10 mV/s. The frequency correlation of ionic bipolar rectification was investigated by varying the time intervals (from 0.1 s to 1 s) between successive scanning cycles while maintaining a fixed scan rate at 1 mV/s. All reported *I-V* behaviors for different GITs containing diverse cations and a fixed anion represent the experimentally observed ionic current flowing under applied voltage conditions. All observed ionic current and rectification behaviors are fundamentally determined by the net ionic flow arising from the cooperative migration of both cations and anions across the cascade-heterointerfaces. The forward rectification ratio (f) was calculated as $f = |+i_{max}/-i_{max}|$ and the reverse rectification ratio (f') was calculated as $f' = -|-i_{max}/+i_{max}|$. The related current density (J) was calculated as $J = i / A$, where A is the GIT cross-sectional area ($A = \pi \cdot (d/2)^2$). Absolute transient current responses of the GIT_{Na} were measured under a constant voltage of ±12 mV. Relaxation behavior of the ionic current was characterised during a voltage scan from 12 mV (or -12 mV) to 0 mV. Long-term rectification stability of the $GIT_{Ca/Al}$ was tested every 2h over 24h under alternating electric fields. The ionic conductivities of GITs were systematically measured using the four-probe method.

Multistate ionic neuromorphic characteristics

The multistate ionic neuromorphic measurements were performed using the Keithley 2636B SourceMeter (Keithley Instruments, Cleveland, OH) and a pair of Ag/AgCl electrodes. The hysteresis loops, cycling stability, paired-pulse test, and retention time were measured on cylindrical GITs with diameters of 250 μm and 100 μm, each with a uniform length of 1.5 mm. GIT_{cation} and GIT_{anion} exhibited the ionic neuromorphic facilitation and depression features, respectively. The hysteresis loops and cycling stability were measured by two-terminal *I-V* scans under alternating electric fields with ranges of ±30 mV and ±40 mV at different scan rates (0.1, 1, and 25 mV/s). The plasticity and memory characteristics were measured using voltage pulse pairs with amplitudes of ±30 mV and ±40 mV, a fixed pulse duration of 10 ms, and a controlled time interval (Δt) of 10 ms. The change of postsynaptic ionic current was calculated as $\Delta i = i_2 - i_1$, where i_1 and i_2 represent the postsynaptic ionic currents generated by the first and second voltage pulses, respectively. Paired-pulse facilitation retention time ($t_{r,PPF}$) and paired-pulse depression retention time ($t_{r,PPD}$) are defined as the time required for the postsynaptic current response, following facilitation or depression induced by paired stimulation, to decay and stabilize back to its baseline steady-state level. Behaviors with retention times ≤ 1 s are classified as short-term (ST) memory, and those > 1 s as long-term (LT) memory. The ionic capacitance was modulated by utilizing GIT materials with differing geometric widths (100 μm and 250 μm) to vary the surface area of the centre-heterointerface with uniform sub-heterointerface density and heterostructure. Consequently, narrower (100 μm) GIT samples displayed clear ST memory characteristics, whereas wider (250 μm) samples exhibited pronounced LT memory behaviors. LT-type GIT systems can be dynamically modulated to exhibit ST behavior by adjusting the amplitude of input voltage pulses. In contrast, ST-type GIT

systems cannot transition to LT behavior due to inherently limited heterointerface-trap strength. Under the same pulsing conditions, repeated stimulation with 10 consecutive pulses was applied to evaluate the progressive evolution of the t_r. The plasticity factor (k), defined as the slope of t_r with respect to the amplitude of the spike voltage. Conductance (G) is calculated using Ohm's law based on the peak value of postsynaptic ionic current (i) measured under a specific spike voltage (V): $G = i / V$. The neuromorphic energy consumption during per single spike pulse was calculated according to the equation $W=Vit$, where V represent the spike voltage, i represent the postsynaptic ionic current, and t represent the pulse time, respectively.

Hebbian, anti-Hebbian, and BCM learning rules. We demonstrate the Hebbian learning rule in the $GIT_{Ca/Al}$ system and the anti-Hebbian learning rule in the $GIT_{Cl/ClO}$ system. We applied a sequence of four consecutive voltage pulses comprising two positive and two negative pulses with controlled time intervals (Δt), using amplitudes of ±30 mV and ±40 mV and a fixed pulse duration of 10 ms. The Δt was systematically varied between -100 ms and +100 ms to simulate different positive and negative pulse sequences. The resulting change in synaptic connection strength (ΔG) was calculated as $\Delta G = (G_F - G_O)/ G_O$, where G_O and G_F represent the conductance values measured under the original and final spikes. For BCM learning rule measurements, we integrated both the $GIT_{Ca/Al}$ and $GIT_{Cl/ClO}$ systems into a dual-crossbar configuration. We then applied periodic alternating voltage pulses with an amplitude of ±30 mV, a fixed pulse duration of 10 ms, and a fixed time interval of 10 ms to emulate synaptic activity. Subsequently, we applied periodic voltage pulses of +30 mV with a duration of 10 ms at varying frequencies from 1 to 100 Hz to induce the change of synaptic connection strength. Before each frequency-dependent test, the device was initialized to a defined conductance state (G_O = 1, 2, or 3 μS) by applying a sequence of pre-conditioning

pulses. The final conductance (G_F) was recorded 1 s after the frequency stimulation.

Molecular dynamics simulation and experimental characterization of heterointerface-traps

According to the chemical composition and structural features of the GIT, the molecular dynamics (MD) model of the heterointerface between AEP, RMP, and CEP was constructed in a 70 × 70 × 180 Å box. The Optimized Potentials for Liquid Simulations (OPLS) force field was used in the MD simulations, incorporating the TIP3P potential model for water and Al^{3+},[1-3]. Geometric mixing rules were applied to determine the Lennard-Jones parameters. The SHAKE algorithm was employed to constrain the geometry of water molecules with an accuracy of 10^{-4}, while the particle-particle particle-mesh (PPPM) method was used for long-range electrostatic interactions with the same accuracy[4]. Periodic boundary conditions were applied in the x- and y-directions, while fixed boundaries with vacuum layers at both ends were introduced in the z-direction to separate the AEP and CEP sections and prevent atoms from moving out of bounds. The GIT system was equilibrated under the NPT ensemble at 300 K and 1 bar for 2 ns. The equations of motion were solved using the Verlet leapfrog algorithm with an integration timestep of 1 fs. A Nose-Hoover thermostat with a damping time of 0.1 ps and a Nose-Hoover barostat with a damping time of 1 ps were used during the equilibration process. Subsequently, the energy barriers for ion transmission were analyzed. All MD simulations were conducted using the Large-scale Atomic/Molecular Massively Parallel Simulator (LAMMPS)[5].

Free-energy analysis methods. The transfer energy barriers of free ions crossing the heterointerfaces were obtained from the potential of mean force (PMF) calculated using the umbrella sampling (US) method. In the study of transfer energy barriers, the

transmission path was defined along the z-axis, spanning from AEP through RMP to CEP, with sampling points placed at uniform intervals of 0.5 Å along the path. At each sampling point, a harmonic potential with a stiffness of 1 kcal / (mol·Å^2) was applied in the z-direction, and 0.25 ns of sampling was performed under the NVT ensemble. The weighted histogram analysis method (WHAM) was used to compute the PMF curve, providing an estimate of the energy profile along the transmission path. For Na^+, Ca^{2+}, and Al^{3+}, six sets of samples were collected respectively, and the average was taken as the energy profile for ion transmission. WHAM calculations were performed using the g_wham program[6].

Relaxation-time energy spectrum. The relaxation-time energy spectrum measurements were performed using a workstation (CT2001B-A2) on a cylindrical GIT_{Na} with a diameter of 250 μm. The relaxation-time energy spectrum was obtained by analyzing the centre heterointerface-related region (~5 μm) of the GIT_{Na}. A voltage bias was applied and swept from 12 mV to 0 mV at a scan rate of 1 mV s^{-1}. Upon reaching 0 mV, the external electric field was removed, and the subsequent relaxation process was continuously recorded with in a time window of 12.4s. The obtained relaxation curves were fitted using multi-exponential decay functions to extract characteristic relaxation time constants, which were further used to construct the relaxation-time energy spectra.

Characterization of microstructure

The microstructures of the GIT were characterised using a confocal laser scanning microscopy (CLSM, Olympus FV31S) and a scanning electron microscopy (SEM). The size distributions of polyelectrolyte disperse-phases were analyzed by dynamic light scattering (DLS).

Measurements of mechanical properties

Loading and compressive tests of the samples were performed on a tensile-compressive tester (CTM2100, Xieqiang Instrument Technology Co., China). In the test, cylinder-shaped (10 mm diameter × 10 mm height) samples were measured with applied compression strain (0-80 %) at a constant compression rate of 8 mm/min. The elastic modulus (E) was calculated from the slope of the stress-strain curves between 0-30% deformation.

Measurements of swelling behaviors

The sample was immersed in deionized water at room temperature, then was taken out and weighed daily for 7 days. The equation of swelling ratio is as follows:

$$\text{swelling ratio} = W_x / W_o \times 100\%$$

where W_x and W_o refer to the weight of the swelling and original samples, respectively.

Measurements of dehydration resistance behaviors

The sample was placed in the air (RH = 20%) at room temperature and then weighed daily for 7 days. The equation of dehydration ratio is as follows:

$$\text{Dehydration resistance ratio} = W_1 / W_o \times 100\%$$

where W_1 and W_o represent the weight of the dehydrated and original samples, respectively.

Measurement of inductive coupled plasma emission spectrometer

Transmitted ionic signal strengths (ion concentration) of the samples were characterised using a pair of Pt electrodes. Both tanks were filled with the GIT samples and DI water. For this experiment, GIT_{Na} and $GIT_{Ca/Al}$ were used. Ionic signals of the GITs were

monitored under unidirectional rectification and bipolar rectification processes. After each stimulation period (2 h), the solution was collected, and the tank was refilled with DI water. The ion concentrations of the collected solutions were measured using inductive coupled plasma emission spectrometer measurement (ICP, NexION 1000).

Calculation of the activation energy

The ionic conductivity of the GITs, polyanion electrolyte hydrogels (AEP) and polycation electrolyte hydrogels (CEP), containing mobile Na^+ and Cl^- ions, was measured over a temperature range of 20 - 80 °C under identical experimental conditions. The AEP and CEP systems corresponded the polyanion and polycation electrolyte components of GIT systems, respectively. The activation energy (E_a) of the mobile Na^+ and Cl^- ions in the GIT, AEP, and CEP was calculated based on the Arrhenius relationship:

$$ln\sigma = ln\sigma_0 - \frac{E_a}{RT}$$

where σ is the measured ionic conductivity, σ_0 is the pre-exponential factor, E_a is the activation energy, R is the constant (8.314 J mol^{-1} K^{-1}), and T is the absolute temperature.

Measurement of bioneuron-driven ionic neuromorphic processing

The biohybrid neural circuit was constructed by physically interfacing a GIT-based neuro-iontronic processor (1.5 mm × 250 μm × 100 μm per channel) with the transected sciatic nerve of anesthetized rats via 3D-printed PEDOT:PSS hydrogel bioneural electrodes (1 mm × 100 μm × 100 μm). Electrophysiological recordings of original (pre-transection) and upstream (post-transection) neural spike signals were performed to confirm their equivalence and establish baseline references. The upstream neural activities were generated by a typical rhythmic tail-pinch protocol in rodent models.

Reconstructed downstream neural signals processed by the GIT-based neuro-iontronic processors were recorded as biopotentials using PEDOT:PSS hydrogel bioneural electrodes, which were integrated into a synchronized electrophysiological acquisition measurement system. After sciatic nerve transection, we also conducted control experiments without the GIT processor yielded no detectable downstream response. Moreover, we performed neural signal recordings and conducted statistical comparisons across all five rats' neural signals through calculated P-values. All the animal experiments followed the guidelines of the Institutional Animal Care and Use Committee and Ethics Committee of Capital Medical University. The rats were anesthetized with 1-3% isoflurane in oxygen (5ml/kg, N914855, Shanghai Macklin Biochemical Co., Ltd., China) and fixed in the supine position on the operating table. Skin incision was created on the thigh after shaving. A 0.5 cm incision was introduced parallel to the femur approximately 1.5 mm anterior to the femur. Hamstring muscles were located and separated using autoclaved sharp sticks to allow access to the sciatic nerve. The sciatic nerve was firmly held using hemostatic forceps (Fine Science Tools, 13020-12), and then ~5 mm of the nerve was transected using fine sterile scissors. Data were analyzed using one-way ANOVA followed by Tukey's post hoc test and are presented as the means ± SDs. ns $p > 0.05$, **$p < 0.01$ compared to the control group. $n = 3$

Cell viability measurement, live/dead staining

The biocompatibility was assessed by using the cell counting kit-8 (CCK-8, Solarbio, CA1210) method. Briefly, cells were seeded into 96-well plates and co-cultured with the aseptically processed GIT for 1 day, 3 days, and 7 days. After that, remove the GIT, then added 10% CCK-8 solution to cells. After incubation at 37 °C for 1 h, the optical

density (OD) was measured by an absorbance microplate reader at 450 nm.

The cell viability was expressed as a percentage of treated groups of the control group. Each sample was evaluated in triplicate. For further biocompatibility evaluation, Calceiin-AM/EthD-III live/dead double staining kit (Solarbio, CA1632) was performed. According to the manufacturer's instruction, the images of staining samples were taken by fluorescence microscope. Numbers of live and dead cells in images of each day were counted using ImageJ.

Histology and immunohistochemistry evaluation

Before implantation, all GITs were first rinsed with sterile saline and then sterilized by exposure to xenon light irradiation for 10 min. The GITs were then implanted subcutaneously into the dorsal region of healthy adult SD rats, and the incisions were sutured. The rats were maintained for 2 weeks, after which they were euthanized under anesthesia for tissue collection. Another six healthy age-matched rats that underwent sham surgery were raised as controls. Following the 2-week period, the liver, spleen, and kidney tissues of the rats were stained with hematoxylin-eosin (H&E) to assess the overall tissue architecture and potential inflammatory cell infiltration.

Fluorescence imaging

For Ca^{2+} imaging within the $GIT_{ca/Al}$ channel, the calcium-specific fluorescent probe (Fluo-4) was prepared by dissolving it in Pluronic F-127 (0.1% w/v) and diluting it to a working concentration of 5-10 μM in PBS buffer. The probe was evenly applied to the gel sample to ensure sufficient penetration and was placed in the dark for 30 minutes to 1 hour to allow effective binding to calcium ions. Finally, sequential images capturing Ca^{2+} cross-interface transmission within the $GIT_{ca/Al}$ channel, driven by

upstream neural potential spike signals, were recorded at 20 s intervals.

Electromyographic Measurement

The animals were anesthetized (1-3% isoflurane in oxygen). Three skin incisions were created. The first skin incision was on the leg of a rat to implant two electrodes on the biceps femoris. The second one was on the head to fix a head connector. Two holes were drilled on the skull using a microdrill (78001, RWD) and two screws were screwed in the skull. The head connector was placed on the screws and the fixation was done by curing bone cement between the plastic connector and the screws. The third incision was on the back, where the wires from the electrodes were connected to the wire from the head connector. The wires were threaded through the subcutaneous space which was created by blunt dissection. The incisions were then closed by sutures. Electromyographic (EMG) signal was measured by connecting the head connector to a micro-4 system (Cambridge Electronic Design Limited) and recording when the animal was stimulated. We also performed EMG recordings and conducted statistical comparisons across all five rats' EMG signals through calculated P-values (one-way ANOVA with post-hoc Tukey test). Data were analyzed using one-way ANOVA followed by Tukey's post hoc test and are presented as the means ± SDs. ns $p > 0.05$, **$p < 0.01$ compared to the control group. $n = 3$

Section 2: Supplementary Information Note

1. Equivalent capacitance-resistance model of cascade-heterointerface-traps

To explain the cascade-heterointerface-trap effects, the ion transmission process in GITs under applied electric filed is simulated using a continuum model. Initially, we employed the Fokker-Planck equation to model ion migration and diffusion in a cascade free energy landscape. For a 1D concentration field $p(x)$, we had

$$\frac{\partial p(x)}{\partial t} = -\frac{\partial}{\partial x}[v(x)p(x)] + \frac{\partial^2}{\partial x^2}[Dp(x)]$$

where D is the diffusion coefficient assumed to be constant, and

$$v = \frac{D}{k_{\mathrm{B}}T}\left[E_0 q - \frac{\partial V_{\mathrm{Y}}(x)}{\partial x}q - \frac{\mathrm{d}\mu(x)}{\mathrm{d}x}\right]$$

is the migration velocity induced by an applied electrical field $E_0 = V / L$, where V is the applied alternating electric field and L is the length of the simulated region. μ is the chemical potential. Charge q is $-e$ for anions and e for cations. The screened interaction between ions is described by the Yukawa potential

$$V_{\mathrm{Y}}(x) = \int \frac{2\pi g^2}{\alpha}\rho(x')e^{-\alpha|x-x'|}\mathrm{d}x'$$

which can be integrated from the charge density profile.

$$\rho(x) = [ep^+(x) - ep^-(x)]$$

Here g and α are scaling factors (strength and reciprocal of characteristic length) of Yukawa potential and e is the elementary charge.

The ionic currents during forward or reverse voltage scans are calculated from the above Eqs. using finite difference (FD) methods. An explicit forward time central space scheme is used to solve the time evolution of ion concentration on a one-dimensional grid. Convergence of the simulation is verified by comparing results under different time steps and grid densities. The chemical potential profile represented the biphasic

structure, with smoothing applied to the CEP/AEP-RMP (C/A-R) boundaries. $\Delta\mu_C$ is the chemical potential difference between the centre-heterointerface, while $\Delta\mu_{AEP}$ and $\Delta\mu_{CEP}$ are the energy barriers of AEP sub-heterointerfaces and CEP sub-heterointerfaces, respectively. For simplicity we assume that $\Delta\mu_{AEP} = \Delta\mu_{CEP} = \Delta\mu_C$. The boundaries are in the middle of the AEP and CEP regions with a fixed ion concentration to represent constant ion concentration far from the centre-heterointerface. The electric field in adjacent RMP region is set to zero to avoid boundary effects on the electric field near the interface. The external voltage is described by a time-varying and spatially uniform electric field. A forward electric field of V = 12 mV is applied until a steady state is reached. Then the voltage is reversed from 12 mV to -12 mV at a constant scan rate of -1 mV/s. The evolution of current density and charge distributions is recorded during the voltage scan. Ion accumulation is characterised by effective ionic capacitance Q in AEP and CEP pockets near the centre-heterointerface.

Additional discussions on the experimental setup that is idealized by applying alternating electric field. It is reasonable to represent the applied voltage as an electric field in the simulation. The Ag/AgCl electrodes used in this work are non-polarizable electrodes. This means that the electrode reactions are sufficiently fast, allowing an electric field to be formed instantaneously when the V is applied. Also, the presence of a continuous current under the applied electric field indicates that the heterogated gel system is conductive, and an electric field driving ion transmission exists throughout the system. By choosing the value $E_0 = V / L$, it is assumed that the V is concentrated in the simulated region near that interface. This is reasonable because the high energy barrier at the centre-heterointerface (ΔE_C) causes a high electric resistance near that interface. If there are not a higher (ΔE_C) compared to $\Delta\mu_C$ voltage would not concentrate near the centre-heterointerface and the electric field near the centre-heterointerface

would be lower than ΔE_0, making it even harder for ions to accumulate in the centre-heterointerface. In this case, the rectification effect would not occur. As the rectification effect occurs, ΔE_C is higher than $\Delta \mu_C$, causing V to be concentrated at the centre-heterointerface.

When the alternating electric field scans from $+V$ to $-V$, the system exhibits two states:

(a). Charging states: At $V = +V$, ions migrated rapidly under high voltage and formed anion and cation accumulation on both sides of the high interface energy barrier. The strong electrostatic interaction formed by the accumulation of high concentrations of anions and cations forms a continuous current across a high energy barrier, and the direction of the built-in ionic potential field was consistent with the direction of $+V$.

(b). Discharge state: When the voltage changes to $-V$, the applied electric field is difficult to maintain the accumulative effect of ions, and the accumulated ions are gradually dissipated to both sides. The current cause by electrostatic interaction weakens but remains in the same direction.

Therefore, the overall current can be divided into two parts. One part is the pure resistive network current caused by the resistance effect of the energy barrier, and the other part is the enhanced electrostatic interaction effect resulting from ion accumulation at the centre-heterointerface.

To describe the system's rectification effect, we introduce a capacitance model with a leakage effect and constructed an equivalent resistance model. The ion accumulation effect at the heterointerface is equivalent to a non-ideal capacitance, in which the high energy barrier is equivalent to a non-ideal dielectric with high resistance, allowing leakage current to pass. The electric field between the capacitor plates accelerated the migration of ions. In this model, changes in ion concentration due to the ionic current are neglected.

Under the influence of a high electric field, the capacitor charges rapidly. Once the circuit reaches a steady state, the capacitor's built-in electric field accelerates the charge carriers through the resistor (R_T), thereby influencing the current in pure resistance systems. The total current can be written as:

$$I = I_1 + I_2$$

$$I_1(t=0) = \frac{V}{\sum_1^n(R_n) + \sum_1^m(R'_m) + R_T}$$

$$I_2(t=0) = \frac{Q(t=0)}{CR_T} = \frac{\frac{R_T V}{\sum_1^n(R_n) + \sum_1^m(R'_m) + R_T}}{R_T} = \frac{V}{\sum_1^n(R_n) + \sum_1^m(R'_m) + R_T}$$

Here, I_1 is the response current generated by the resistor network to voltage, and I_2 is the carrier migration current induced by the built-in electric field generated by the capacitor. R_n and R_m represent the resistance of the respective AEP and CEP sub-heterointerfaces.

After completing the charging process, as the voltage decreases, the capacitor gradually discharges and the built-in electric field weakens, and I_2 decreases.

$$I_2(t) = \frac{Q(t)}{CR_T}$$

To simplify the model, we expressed the change of the charge on the capacitor with time as,

$$Q(t) = Q(t=0)\left(e^{-\frac{t}{t_0}}\right)$$

t_0=RC is the capacitor charge and discharge time constant, in which

$$R = \frac{1}{\frac{1}{\sum_1^n(R_n) + \sum_1^m(R'_m)} + \frac{1}{R_T}}$$

$$C = \frac{Q(t=0)}{\frac{R_T V}{\sum_1^n (R_n) + \sum_1^m (R'_m) + R_T}}$$

When the voltage scan time was much longer than the capacitor response time, the total current ($I(t)$) can be expressed as

$$I(t) = I_1(t) + I_2(t)$$

$$= \frac{V(t)}{\sum_1^n (R_n) + \sum_1^m (R'_m) + R_T} + \frac{\left(e^{-\frac{t}{t_0}}\right) \frac{R_T V}{\sum_1^n (R_n) + \sum_1^m (R'_m) + R_T}}{R_T}$$

Considering the high energy barrier at the heterointerface can bring significant ion accumulation effect.

$$R_T \gg \sum_1^n (R_n) + \sum_1^m (R'_m)$$

$$C = \frac{Q(t=0)}{V}$$

The total current ($I(t)$) can be simplified as,

$$I(t) = \frac{V(t)}{R_T} + \frac{\left(e^{-\frac{t}{[\sum_1^n (R_n) + \sum_1^m (R'_m)] \frac{Q(t=0)}{V}}}\right) V}{R_T}$$

The currents of the system under $+V$ and $-V$ are respectively,

$$I(+V) = \frac{V}{R_T} + \frac{V}{R_T}$$

$$I(-V) = (-1 + e^{-\frac{t_{max}}{[\sum_1^n (R_n) + \sum_1^m (R'_m)] \frac{Q(t=0)}{V}}}) \frac{V}{R_T}$$

t_{max} is the scan time from $+V$ to $-V$.

2. Simulation of rectification ratio

The rectification ratio can be expressed as

$$\text{Rectification ratio} = \frac{2}{1 - e^{-\frac{t_{\max}}{[\sum_1^{\mathrm{n}}(R_{\mathrm{n}}) + \sum_1^{\mathrm{m}}(R'_{\mathrm{m}})]\frac{Q(t=0)}{V}}}}$$

In order to consider the ionic capacitance $Q(t=0)$. We consider the continuous migration of ions in a heterointerface medium.

Based on the conservation of ion flow under steady-state conditions,

$$c_1\mu_1 = c_2\mu_2$$

$$c_2 = \frac{\mu_1}{\mu_2}c_1$$

$$\frac{\mu_1}{\mu_2} = e^{\frac{\Delta E_{\mathrm{T}}}{k_{\mathrm{B}}T}}$$

$$Q = c_2SL = ec_1SLe^{\frac{\Delta E_{\mathrm{T}}}{k_{\mathrm{B}}T}} \propto e^{\frac{\Delta E_{\mathrm{T}}}{k_{\mathrm{B}}T}}$$

$$Q \propto \exp\left\{-T\left[\sum_1^{\mathrm{n}}(R_{\mathrm{n}}) + \sum_1^{\mathrm{m}}(R'_{\mathrm{m}})\right]\right\}^{-1}$$

c_1 is the ion concentration in the two phases (assume c_1=1), c_2 is the ion concentration near the interface of the heterointerfaces (assume c_2=1), S is the cross-sectional area of the material, and L is the length of the water phase near the centre-heterointerface.

So,

$$\text{Rectification ratio} = \frac{2}{1 - e^{ae^{\frac{-\Delta E_{\mathrm{T}}}{k_{\mathrm{B}}T}}}}$$

$$a = -\frac{t_{\max}V}{[\sum_1^{\mathrm{n}}(R_{\mathrm{n}}) + \sum_1^{\mathrm{m}}(R'_{\mathrm{m}})]ec_1SL}$$

Take S = 1 cm^2, L = 1.57 μm, c_1 = 1 mol/L, $t_{\max}$ = 1 s, V = 12 mV, $\sum_1^{\mathrm{n}}(R_{\mathrm{n}}) + \sum_1^{\mathrm{m}}(R'_{\mathrm{m}})$ = 0.08 MΩ for Ca^{2+}.

When ΔE_T= 55 k_BT, rectification ratio is 258.

For a mixed system of 1mol/L Ca^{2+} and 1mol/L Al^{3+}. when the voltage is $+V$, the electric field assists the rapid transport of ions across the interface. At this time, the blockage of ion channels at the heterointerface was ignored. The total current is

$$I_{forward} = I_{forward}(\mathrm{Ca^{2+}}) + I_{forward}(\mathrm{Al^{3+}})$$

$$= \frac{2V}{R_{\mathrm{T}}(\mathrm{Ca^{2+}})} + \frac{2V}{R_{\mathrm{T}}(\mathrm{Al^{3+}})}$$

The change of the charge on the capacitor was caused by diffusion resulted by the differences in ion concentration. The migration rate was slow, and it was easier to form ion blockage. When the channel interfacial retardation ratio of Al^{3+} is α, the current when the voltage sweeps to $-V$ is

$$I_{reverse} = I_{reverse}(\mathrm{Ca^{2+}}) + I_{reverse}(\mathrm{Al^{3+}})$$

$$= \left(-1 + e^{(1-\alpha)a(\mathrm{Ca^{2+}})e^{\frac{-\Delta E_{\mathrm{T}}(\mathrm{Ca^{2+}})}{k_{\mathrm{B}}T}}}\right)\frac{V}{R_{\mathrm{T}}(\mathrm{Ca^{2+}})}$$

$$+ \left(-1 + e^{(\alpha a(\mathrm{Al^{3+}})e^{\frac{-\Delta E_{\mathrm{T}}(\mathrm{Al^{3+}})}{k_{\mathrm{B}}T}}}\right)\frac{V}{R_{\mathrm{T}}(\mathrm{Al^{3+}})}$$

$$R_{\mathrm{T}}(\mathrm{Ca^{2+}}) \propto e^{\frac{\Delta E_{\mathrm{T}}(\mathrm{Ca^{2+}})}{k_{\mathrm{B}}T}}$$

$$R_{\mathrm{T}}(\mathrm{Al^{3+}}) \propto e^{\frac{\Delta E_{\mathrm{T}}(\mathrm{Al^{3+}})}{k_{\mathrm{B}}T}}$$

As $\Delta E_{\mathrm{T}}(\mathrm{Al^{3+}}) \gg \Delta E_{\mathrm{T}}(\mathrm{Ca^{2+}})$ from the molecular dynamics (MD) simulations.

$$R_{\mathrm{T}}(\mathrm{Al^{3+}}) \gg R_{\mathrm{T}}(\mathrm{Ca^{2+}})$$

$$I_{forward} \approx \frac{V}{R_{\mathrm{T}}(\mathrm{Ca^{2+}})}$$

$$I_{reverse} \approx \left(-1 + e^{(1-\alpha)a(\mathrm{Ca^{2+}})e^{\frac{-\Delta E_{\mathrm{T}}(\mathrm{Ca^{2+}})}{k_{\mathrm{B}}T}}}\right)\frac{V}{R_{\mathrm{T}}(\mathrm{Ca^{2+}})}$$

$$\text{Rectification ratio} = \frac{2}{1-e^{(1-\alpha)a(\mathrm{Ca^{2+}})e^{\frac{-\Delta E_{\mathrm{T}}(\mathrm{Ca^{2+}})}{k_{\mathrm{B}}T}}}}$$

Section 3: Supplementary Information Figures

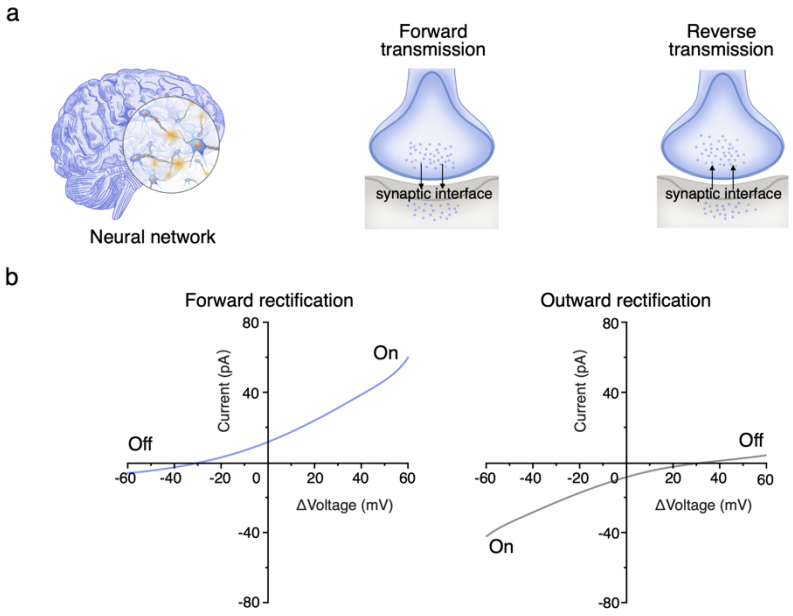

Supplementary Information Fig. 1: Biological synaptic transmission and membrane rectification. a, A bioneural network featuring cascade synaptic architectures. At each synaptic interface, multiple biological signals are transmitted bidirectionally, enabling both forward and reverse transmission. This cascading structure facilitates synergistic effects between synaptic interfaces, enhancing the complexity and functionality of the neural network. **b,** Variations in the membrane potential of nerve cells exhibit characteristics of forward rectification and outward rectification, corresponding to the processes of depolarization and hyperpolarization, respectively.

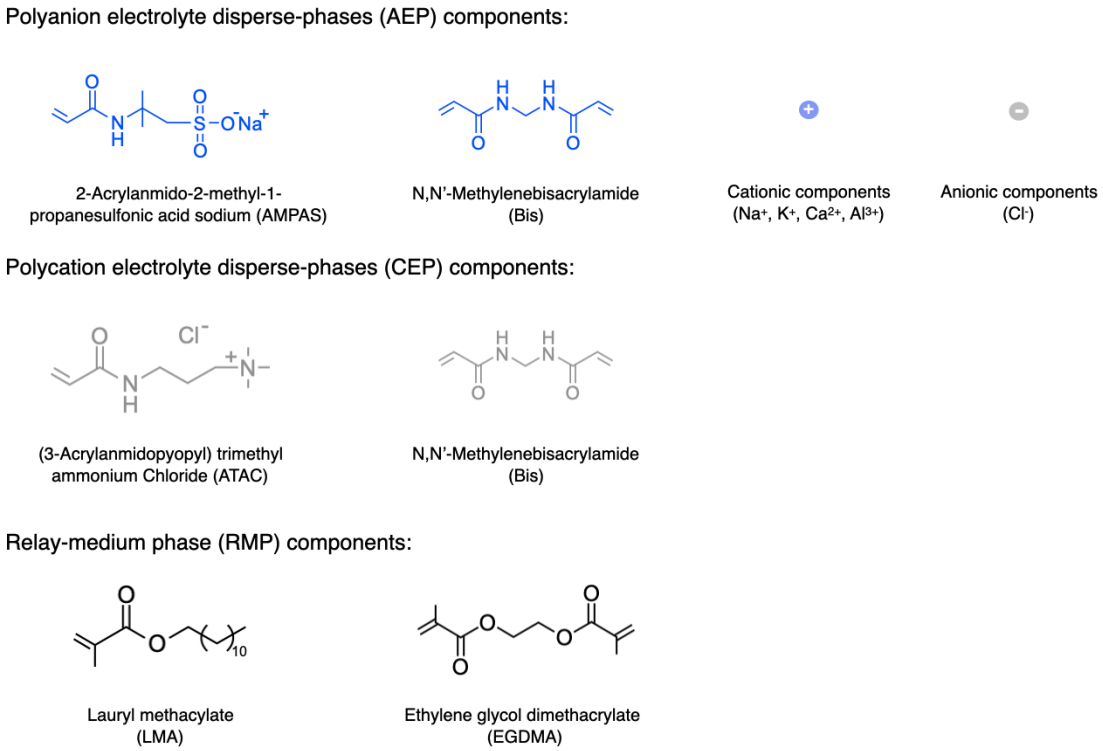

Supplementary Information Fig. 2: Chemical components of the GIT system. The chemical structures of 2-acrylanmido-2-methyl-1-propanesulfonic acid sodium (AMPAS), N,N'-methylenebisacrylamide (Bis), cationic components, anionic components, (3-acrylanmidopyopyl) trimethyl ammonium chloride (ATAC), lauryl methacrylate (LMA), and ethylene glycol dimethacrylate (EGDMA).

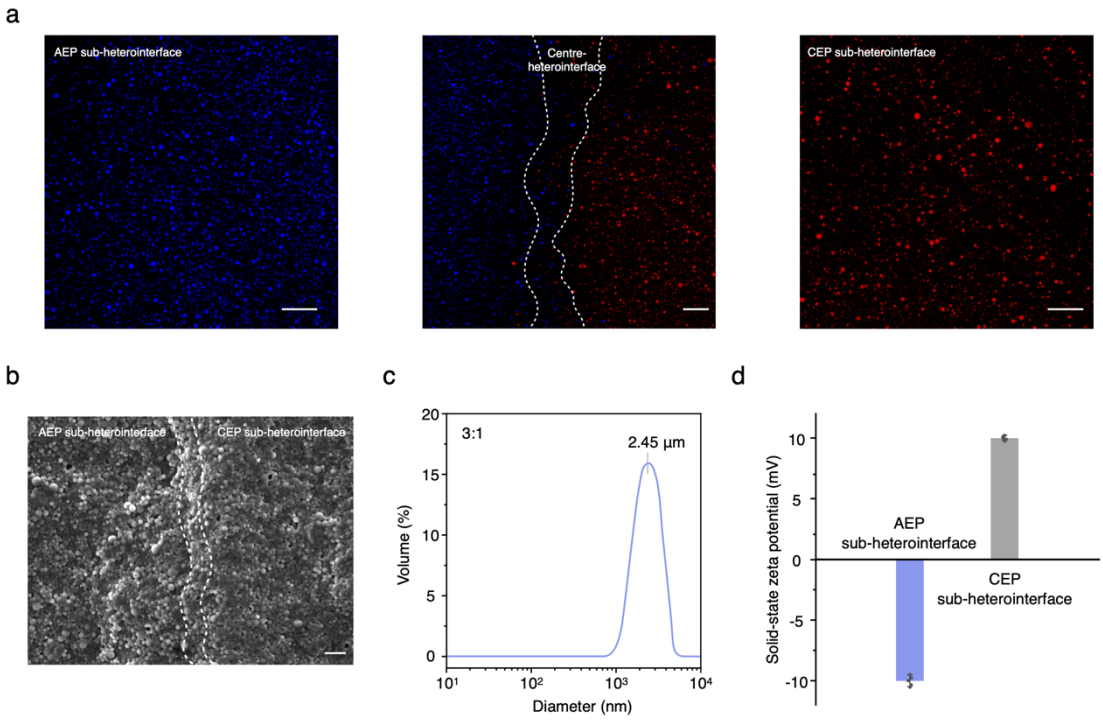

Supplementary Information Fig. 3: Microstructure and interfacial polarity of GITs. a, Confocal laser scanning microscopy (CLSM) images show that the triphase separation structure within the GIT, where AEP (blue-stained) and CEP (red-stained) microinclusions are regionally and uniformly dispersed within the continuous RMP (non-stained) phase. The dashed lines indicate the centre-heterointerface region. Scale bar, 20 μm. **b,** Scanning electron microscopy (SEM) images showing the triphase heterostructures. The dashed lines indicate the centre-heterointerface region. Scale bar, 10 μm. **c,** Size distribution of the polyelectrolyte disperse-phase of the GIT_{Na}. **d**, Solid-state zeta potential of the AEP sub-heterointerface and the CEP sub-heterointerface. Data are presented as mean ± s.d. from 5 independent measurements on the same sample (n = 5).

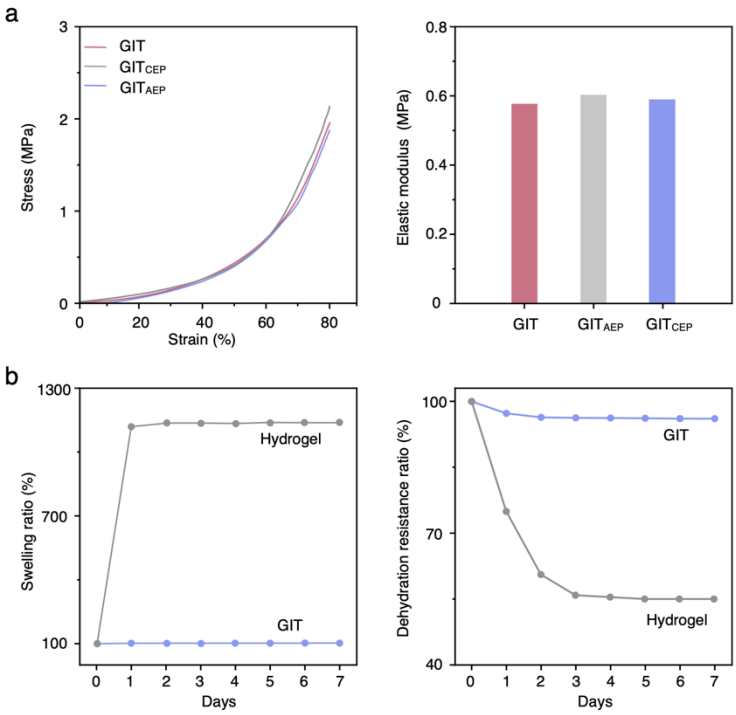

Supplementary Information Fig. 4: Mechanical properties and environmental stability of GITs. a, Compressive stress-strain curves and elastic modulus of the GIT and the sub-heterointerface (i.e. GIT_{AEP} and GIT_{CEP}). The elastic modulus are extracted from the corresponding strain-stress curves. **b,** Swelling and dehydration resistance properties of the GIT and the bilayer polyelectrolyte hydrogel. The data represents continuous measurements from the same sample over 7 days. Therefore, no statistical error bars are shown. Lines are guides to the eye.

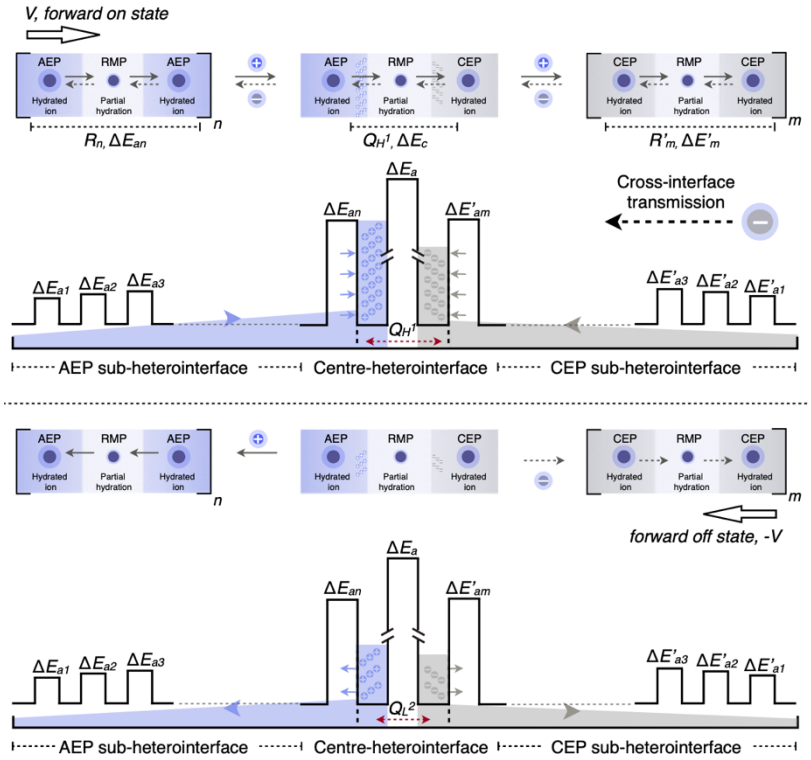

Supplementary Information Fig. 5: Construction and dissipation of anion-dominated heterointerface-traps. The cascade-heterointerface-trap anion transmission under the forward rectification process. ΔE_{an} ($\Delta E'_{am}$) and ΔE_a represent anionic cross-interface transfer energy barriers at the sub-heterointerfaces and the centre-heterointerface. V denotes the applied electric field. Q_H and Q_L denote the effective ionic capacitance during heterointerface-trap construction and dissipation, respectively. The R_n and R'_m represent the resistance of the AEP and CEP sub-heterointerfaces, respectively. n and m denote the numbers of AEP and CEP sub-heterointerfaces. The shaded regions represent the relative strength of heterointerface-traps during ion accumulation and dissipation.

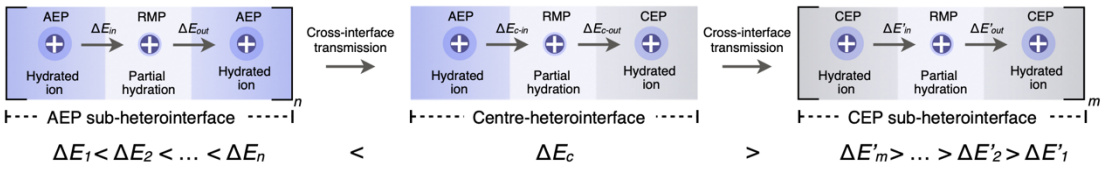

Supplementary Information Fig. 6: Components of cross-interface transfer energy barriers. The total energy barriers for cation transfer within the GIT system can be divided into n+1+m units, corresponding to the sub-heterointerfaces and the centre-heterointerface. For each cross-interface unit, the energy barriers experienced by cations can be further categorized into two components: (1) The energy consumption for transport within the polyelectrolyte disperse-phase and the RMP (ΔE_{in}); (2) The energy consumption for cross-interface transport between the polyelectrolyte disperse-phase and the RMP (ΔE_{out}).

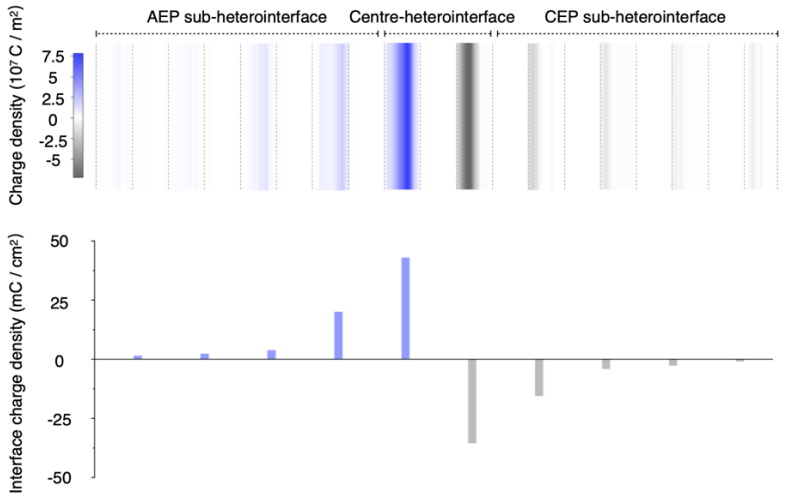

Supplementary Information Fig. 7: Molecular dynamics simulation of ionic accumulation in heterointerface-traps. Simulated cationic and anionic interfacial retardation and corresponding charge accumulation gradients during ionic multiple cross-interface transmission.

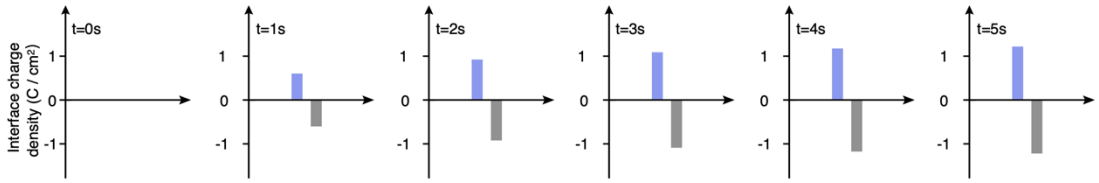

Supplementary Information Fig. 8: Molecular dynamics simulation of temporal heterointerface-trap evolution. Simulated trapped ion charge distribution of the centre-heterointerface over acting time.

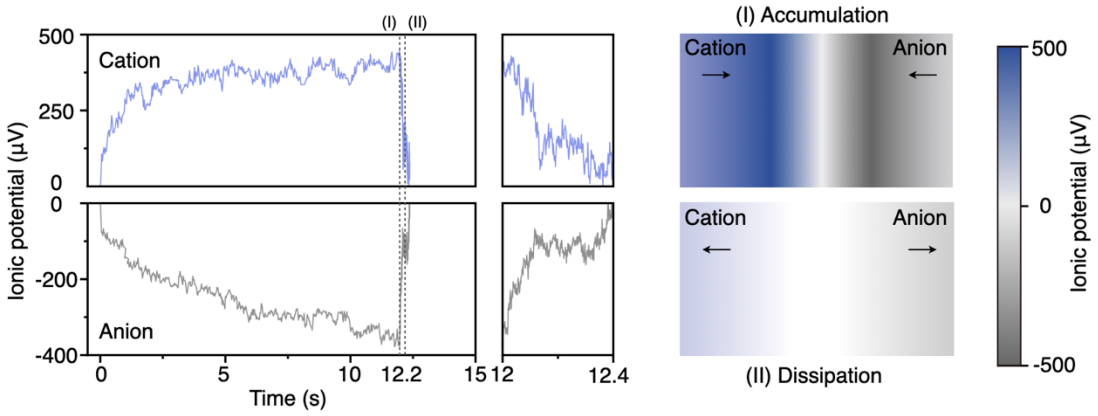

Supplementary Information Fig. 9: Relaxation-time energy spectrum of the centre-heterointerface. Relaxation-time energy spectrum for cross-interface ion transport of the centre-heterointerface-related region (5 μm) within the GIT_{Na} systems, showing asymmetrical cationic and anionic interface distributions and the corresponding dynamic built-in potentials. The dashed lines indicate the boundaries of interfacial ionic relaxation processes within the centre-heterointerface region.

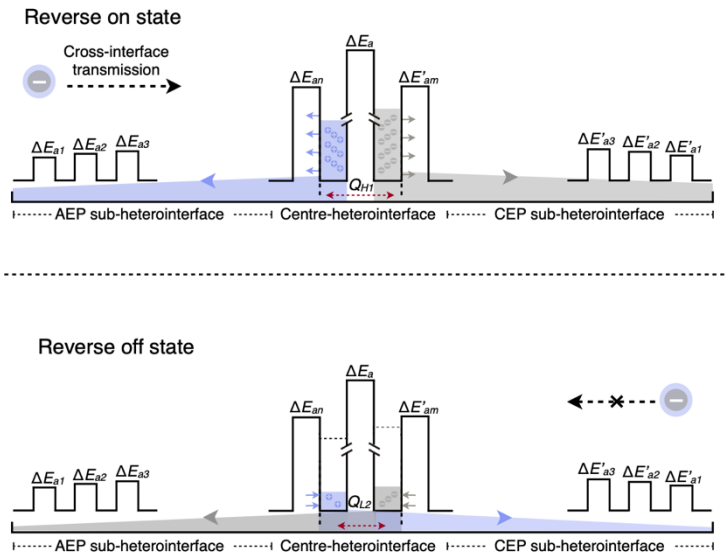

Supplementary Information Fig. 10: Cascade-heterointerface-trap anion transmission during reverse rectification. Schematic illustration of cascade-heterointerface-trap anion transmission under the reverse rectification process. ΔE_{an} ($\Delta E'_{am}$) and ΔE_a represent anionic cross-interface transfer energy barriers at the sub-heterointerfaces and centre-heterointerface, respectively. Q_H and Q_L denote the effective ionic capacitance during heterointerface-trap construction and dissipation, respectively. The shaded regions indicate the relative strength of heterointerface-traps during ion accumulation and dissipation.

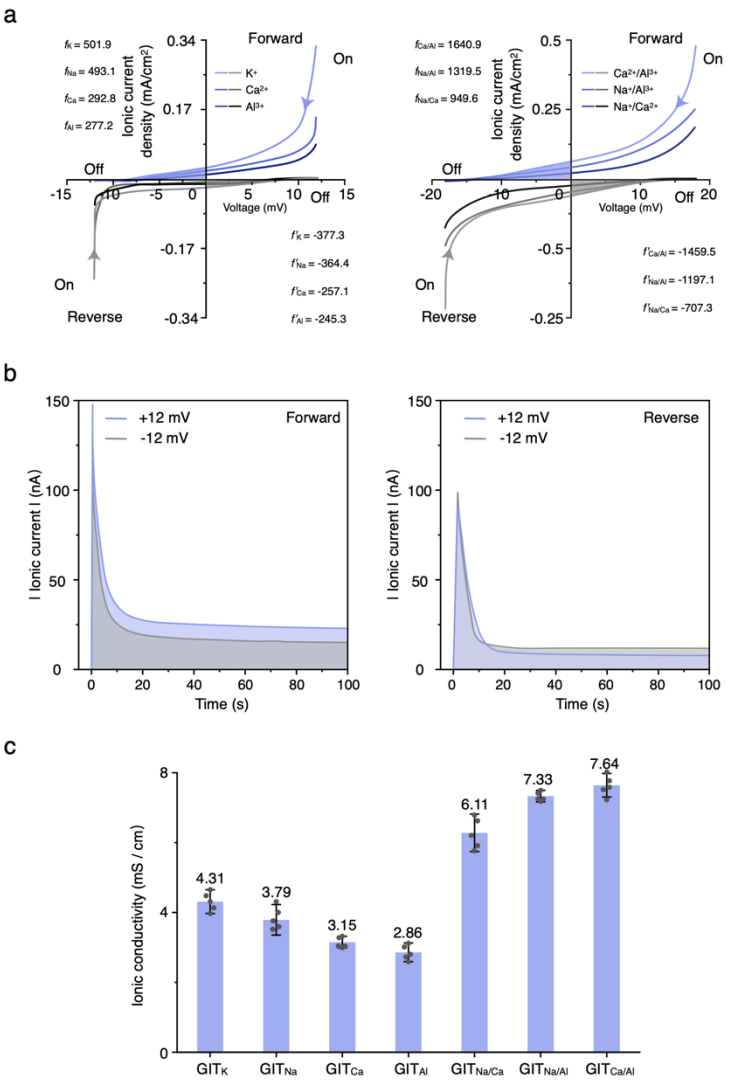

Supplementary Information Fig. 11: Ionic current responses and conductivities of GITs. a, Bipolar asymmetrical current density-voltage curves of GIT systems under alternating electric fields. *f* and *f'* denote the forward and reverse rectification ratios, respectively. The shaded regions indicate the dissipated ion charge capacities. **b,** Absolute transient ionic current response of the GIT_{Na}. The shaded regions represent the areas extracted from the transient ionic current responses.. **c,** Ionic conductivities of GITs configured with different cation species and fixed chloride anions. Data are presented as mean ± s.d. from 5 independent measurements on the same sample (n = 5).

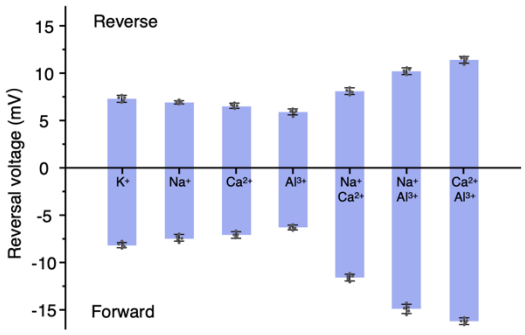

Supplementary Information Fig. 12: Reversal voltage values of GITs containing different monocations and bications during bipolar ionic rectification processes. Data are presented as mean ± s.d. from 5 independent measurements on the same sample (n = 5).

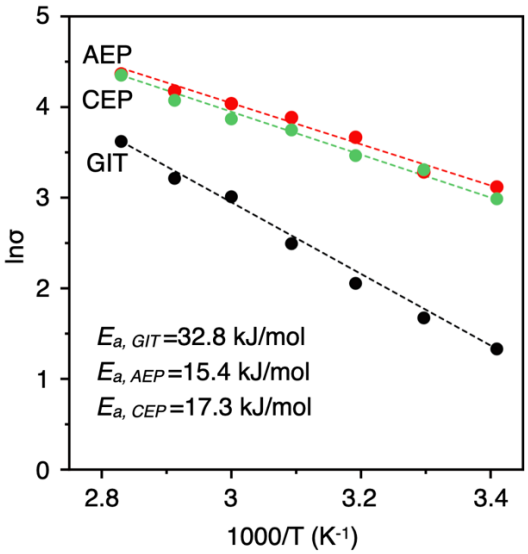

Supplementary Information Fig. 13: Activation energy (E_a) measurements of mobile Na^+ and Cl^- ions in the GIT, AEP, and CEP. Dashed lines represent linear fits based on the Arrhenius equation. The data are obtained from single measurements, and no statistical error bars are shown.

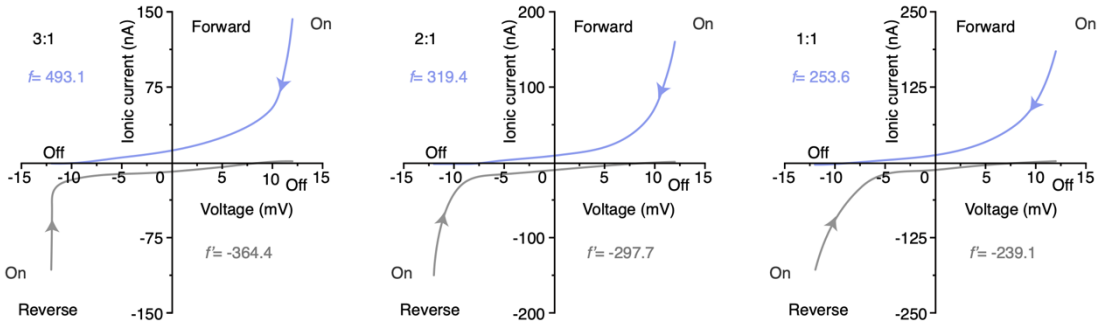

Supplementary Information Fig. 14: Sub-heterointerface density-dependent bipolar rectification of GIT_{Na}. Asymmetrical *I-V* curves of GIT_{Na} under alternating electric fields ranging from 12 mV to -12 mV, indicating the relationship between bipolar rectification ratios and the density of cascade sub-heterointerfaces. The volume composition ratios of the RMP to the polyelectrolyte disperse-phase are 3:1, 2:1, and 1:1, respectively. *f* and *f'* denote the forward and reverse rectification ratios, respectively.

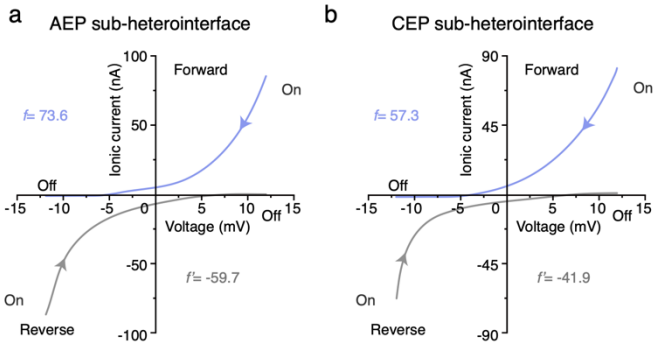

Supplementary Information Fig. 15: Rectification behaviour of isolated sub-heterointerfaces. Bipolar asymmetrical *I-V* curves of the AEP sub-heterointerface **(a)** and the CEP sub-heterointerface **(b)** under alternating electric fields ranging from 12 mV to -12 mV. AEP sub-heterointerface and CEP sub-heterointerface denote the polyanion and polycation electrolyte heterogel components of the GIT system, respectively. f and f' denote the forward and reverse rectification ratios, respectively.

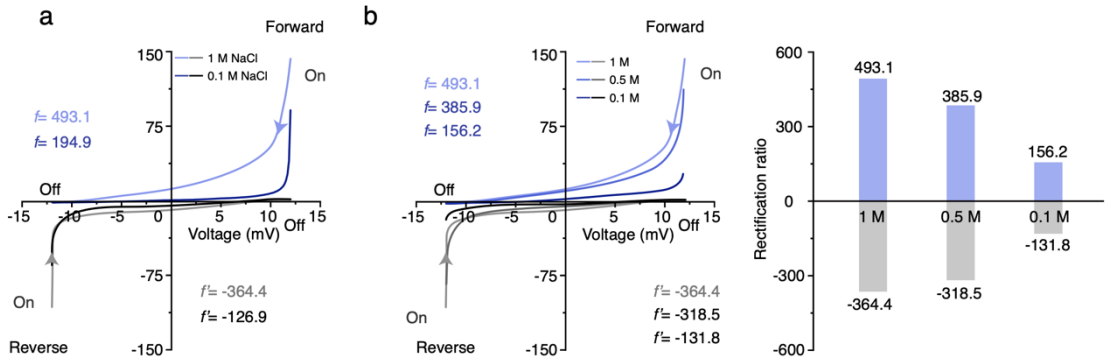

Supplementary Information Fig. 16: Concentration-dependent bipolar rectification of GIT_{Na}. a, Bipolar rectification behaviors of the GIT_{Na} with different ion concentrations. **b,** Bipolar asymmetrical *I-V* curves of GIT_{Na} with varying polyelectrolyte network densities under alternating electric fields. 1 M, 0.5 M, and 0.1 M refer to the molar concentrations of polyelectrolyte monomers in the AEP and CEP precursor solutions, respectively. f and f' denote the forward and reverse rectification ratios, respectively.

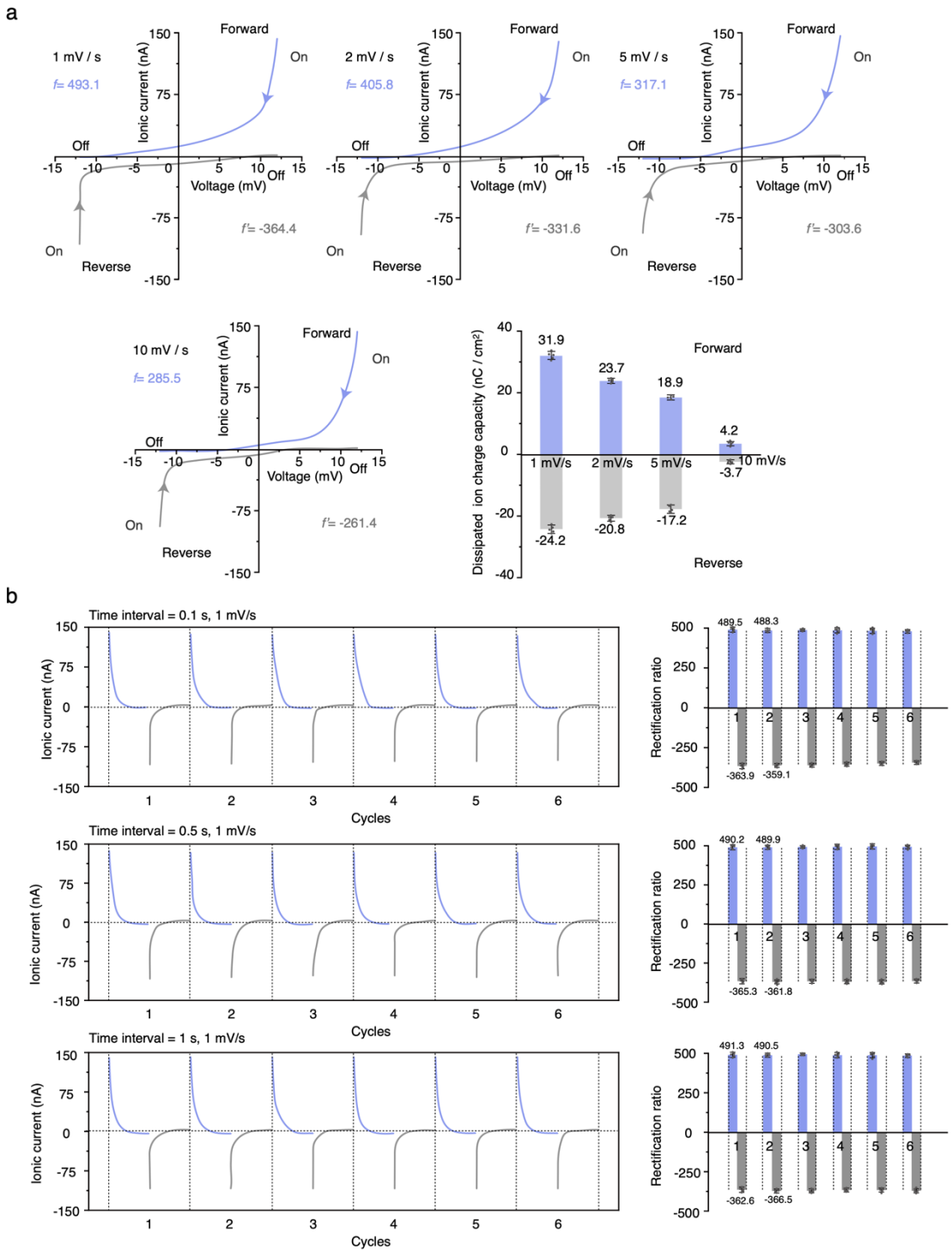

Supplementary Information Fig. 17: Scan-rate and interval dependence of bipolar rectification. a, Bipolar asymmetric *I-V* curves of the GIT_{Na} under varying voltage scan rates (1 mV/s, 2 mV/s, 5 mV/s, and 10 mV/s), and related dissipated ion charge capacities. *f* and *f'* denote the forward and reverse rectification ratios, respectively. Data are presented as mean ± s.d. from 5 independent measurements on the same sample (n

= 5). **b,** Bipolar rectification cycles of the GIT_{Na} under varying time intervals (0.1 s, 0.5 s, and 1 s). Data are presented as mean ± s.d. from 5 independent measurements on the same sample (n = 5).

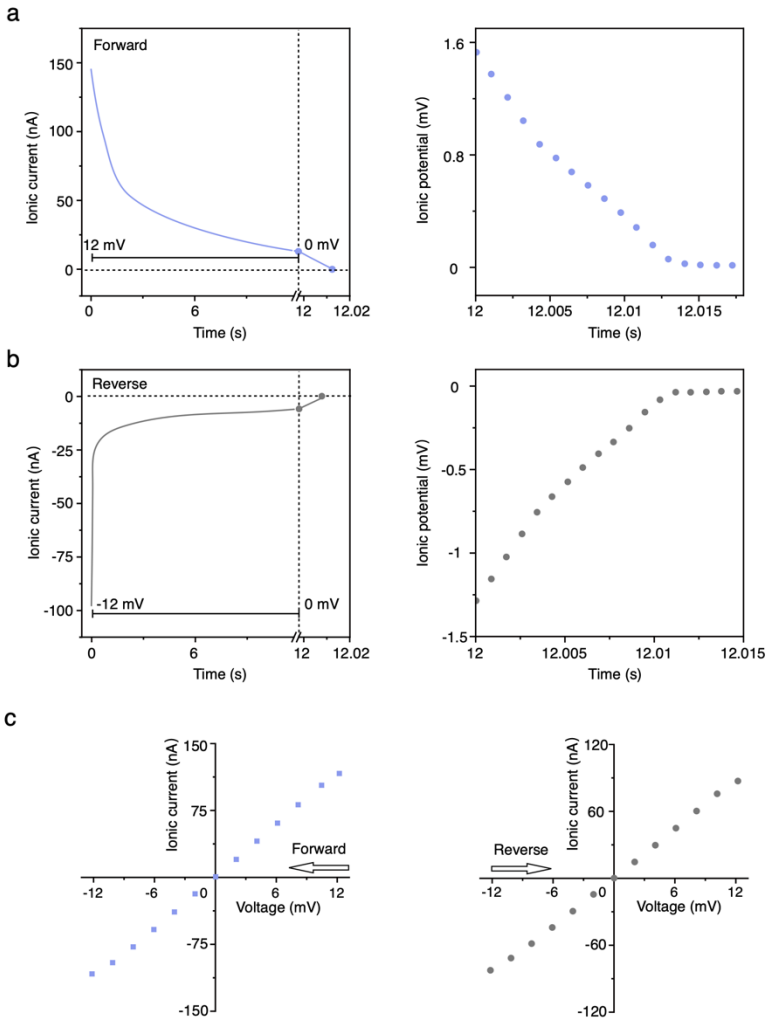

Supplementary Information Fig. 18: Ionic relaxation response of GIT_{Na}. Relaxation time of the ionic current of the GIT_{Na} as the system transitions from a positive (**a**) or negative (**b**) bias voltage scan back to zero voltage, and the corresponding built-in ionic potential near the centre-heterointerface of GIT_{Na}. (**c**) The ionic current response of GIT_{Na} under discontinuous alternating positive and negative electric fields (ranging from 12 mV to -12 mV), with each measurement taken at 10 s intervals. The data represent continuous voltage-sweep measurements from a single device; therefore, no statistical error bars are shown.

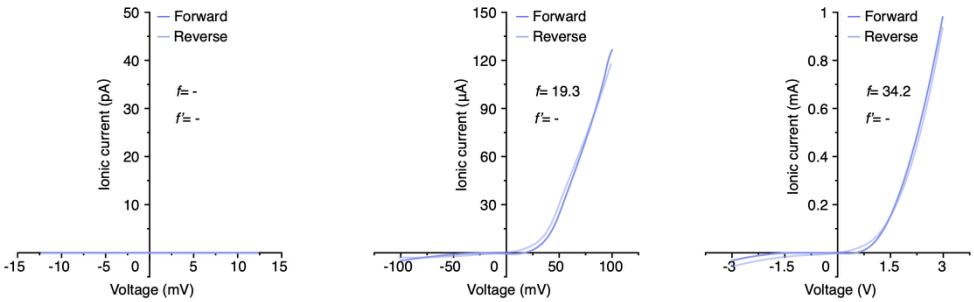

Supplementary Information Fig. 19: Unidirectional ionic rectification behaviors of the bilayer polyelectrolyte hydrogel$_{Ca/Al}$, which requires high driven voltages ranging from 12 mV to 3 V. f and f' denote the forward and reverse rectification ratios, respectively.

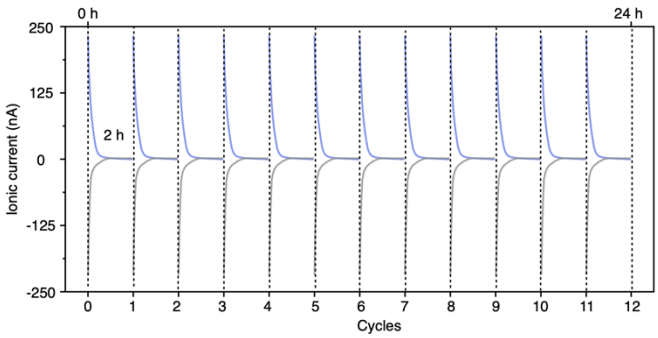

Supplementary Information Fig. 20: Long-term rectified stability of the $GIT_{Ca/Al}$ under alternating electric field cycles tested every 2h within 24h.

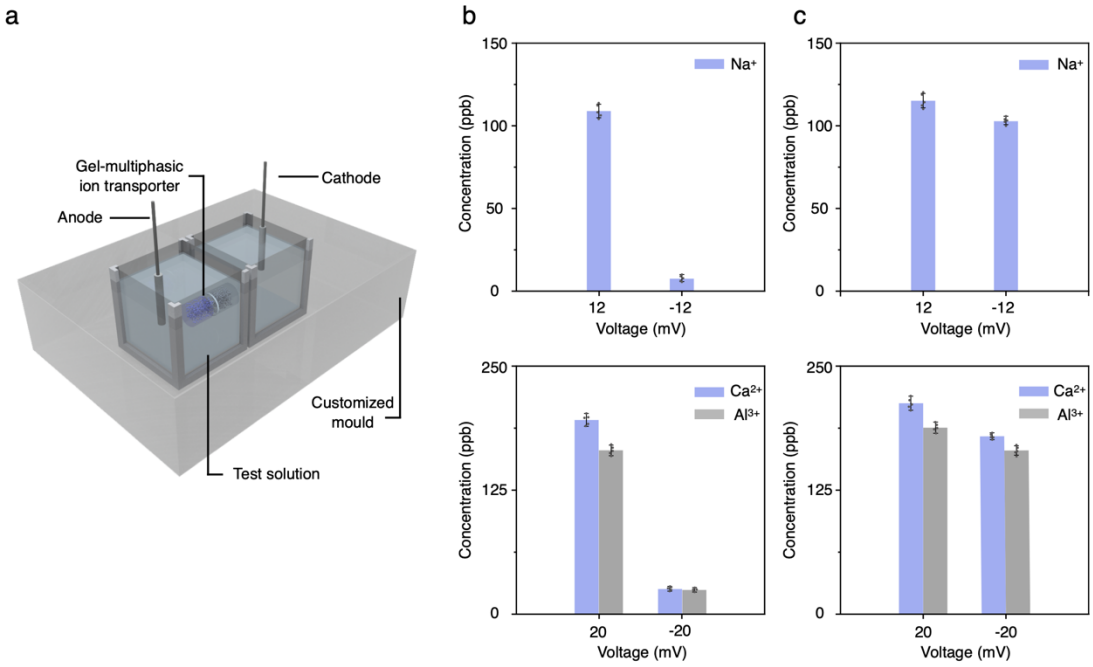

Supplementary Information Fig. 21: ICP analysis of transmitted ionic signals. a, Schematic illustration of the GIT device used for the measurement of inductive coupled plasma emission spectrometer (ICP). (B-C) The transmitted ionic signal strengths of the GIT_{Na} and the $GIT_{Ca/Al}$ under unidirectional rectification (**b**) and bipolar rectification (**c**) processes. Data are presented as mean ± s.d. from 5 independent measurements on the same sample (n = 5).

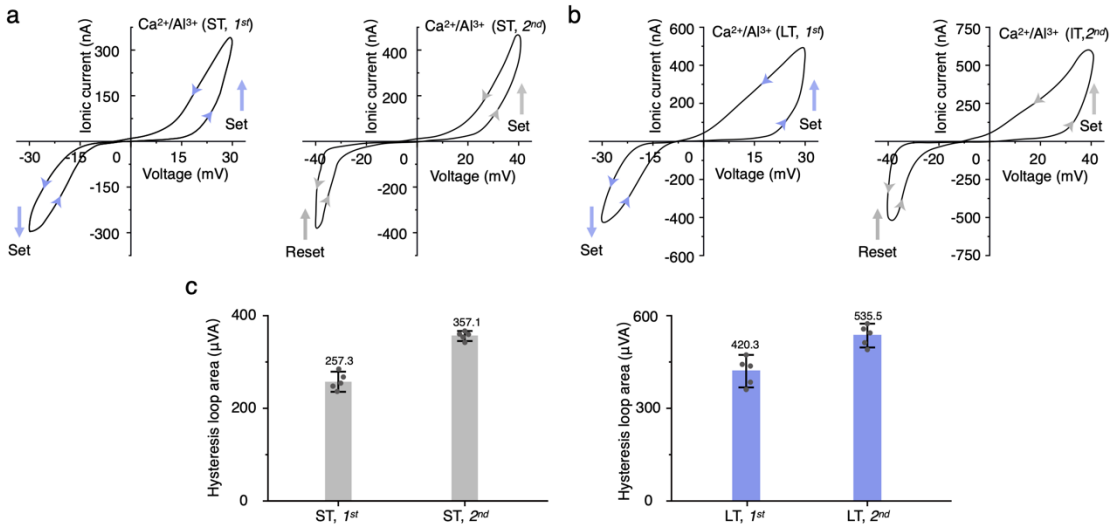

Supplementary Information Fig. 22: Hysteresis loop of dual-order plasticity. Dual-order *I-V* characteristic curves(**a-b**) and hysteresis loop area (**c**) of the $GIT_{Ca/Al}$ with short-/long-term memory features. Data are presented as mean ± s.d. from 5 independent measurements on the same sample (n = 5).

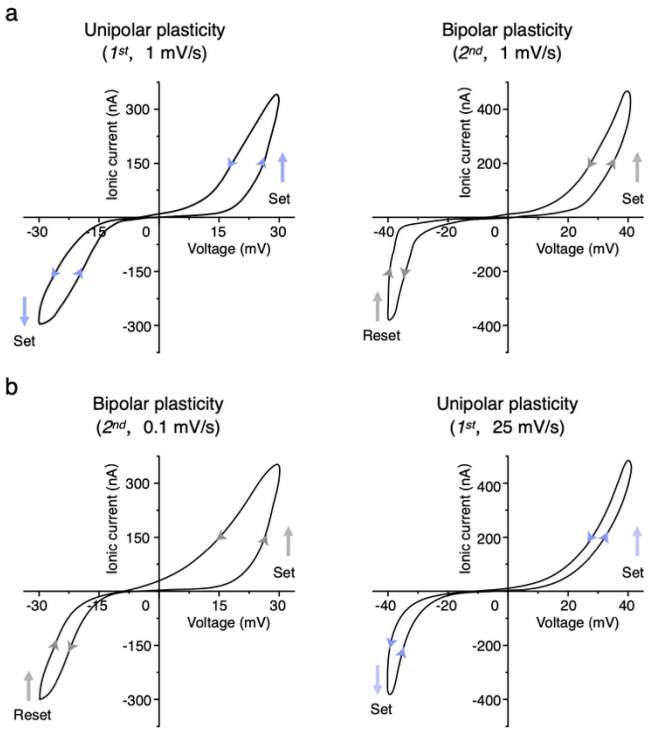

Supplementary Information Fig. 23: Scan-rate-dependent transition between unipolar and bipolar plasticity. Distinct *I-V* characteristic curves of the $GIT_{Ca/Al}$ exhibit the transition between unipolar and bipolar plasticity through adjusting the voltage scan rate.

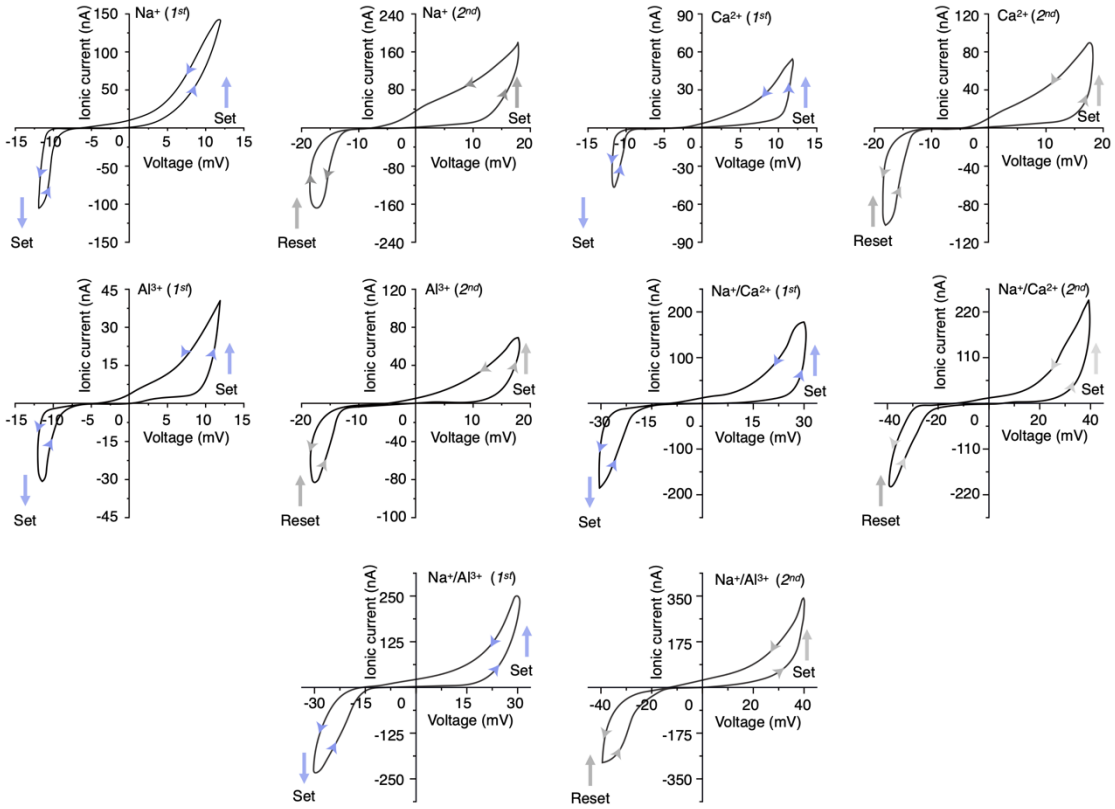

Supplementary Information Fig. 24: Dual-order plasticity of GITs with different ion configurations. Dual-order *I-V* characteristic curves of the GITs containing different monocations and bications with short-term memory.

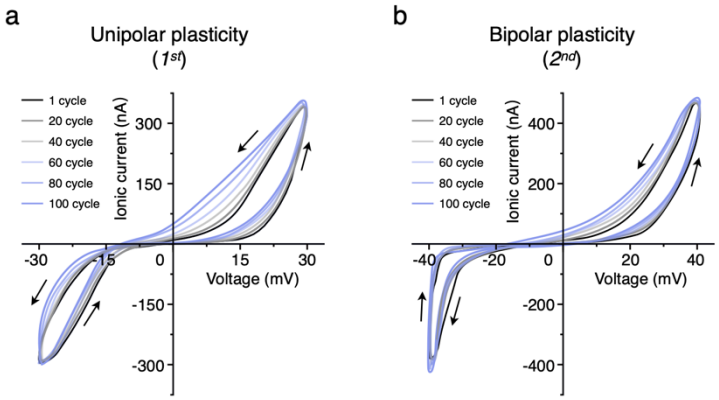

Supplementary Information Fig. 25: Cycling stability of dual-order plasticity. Cyclability of unipolar (**a**) and bipolar (**b**) plasticity of the $GIT_{Ca/Al}$ over 100 consecutive *I-V* cycles (1 mV/s).

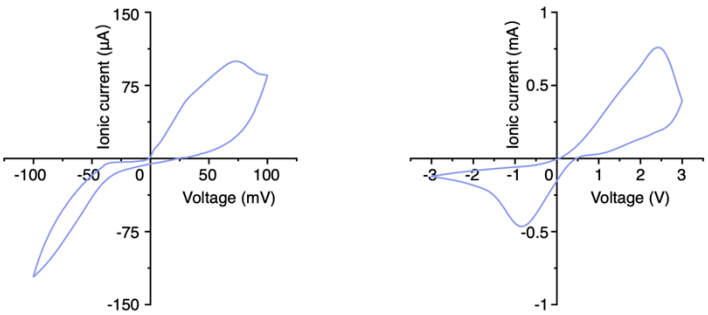

Supplementary Information Fig. 26: *I-V* characteristic curves of the bilayer polyelectrolyte hydrogel$_{Ca/Al}$.

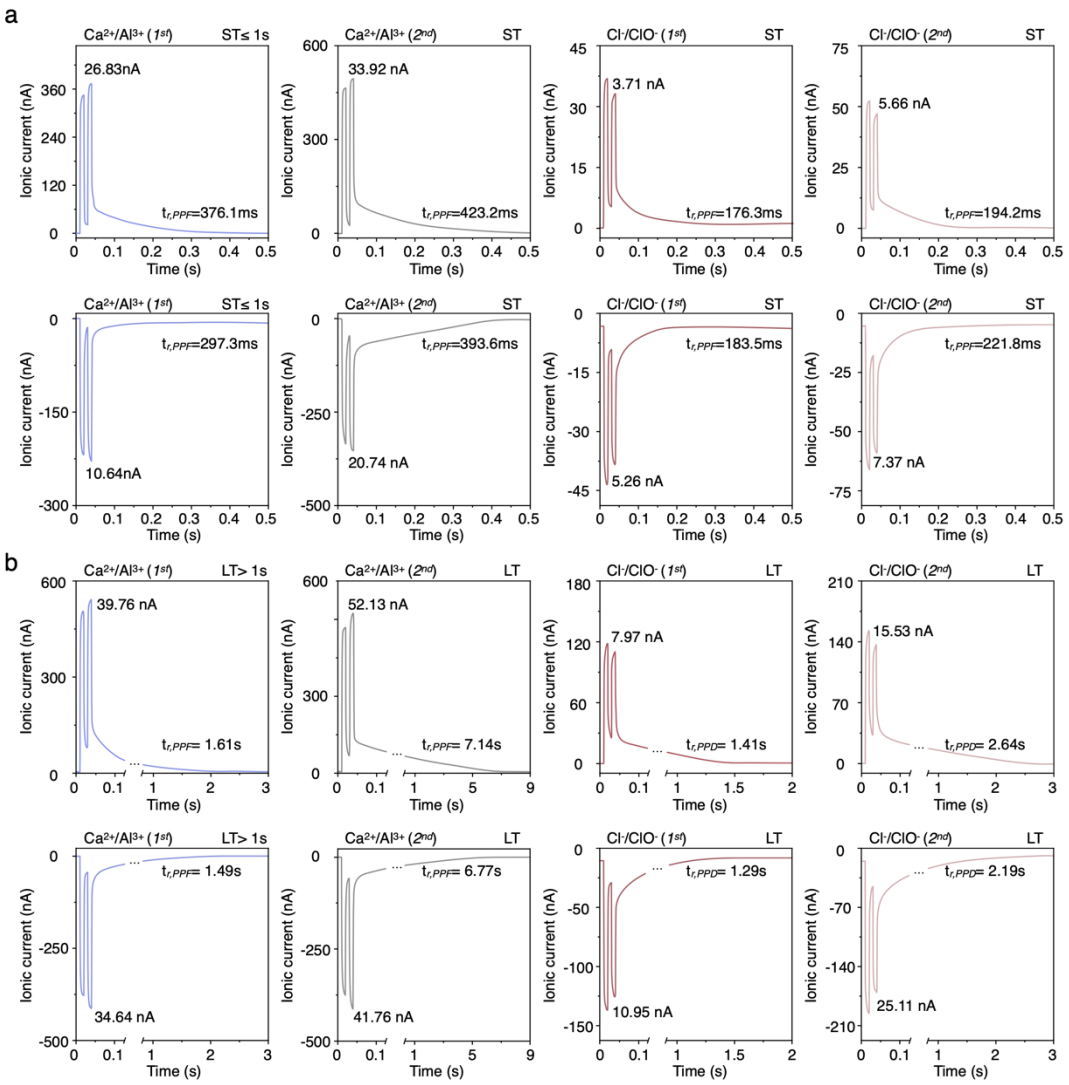

Supplementary Information Fig. 27: Paired-pulse retention features of GIT systems. Paired-pulse ionic current responses of the $GIT_{Ca/Al}$ and the $GIT_{Cl/ClO}$ with short- (ST)/long-term (LT) memory features under varying positive and negative electric field. $t_{r,PPF}$ represents Paired-pulse facilitation retention time ($t_{r,PPF}$) and $t_{r,PPD}$ represents paired-pulse depression retention time.

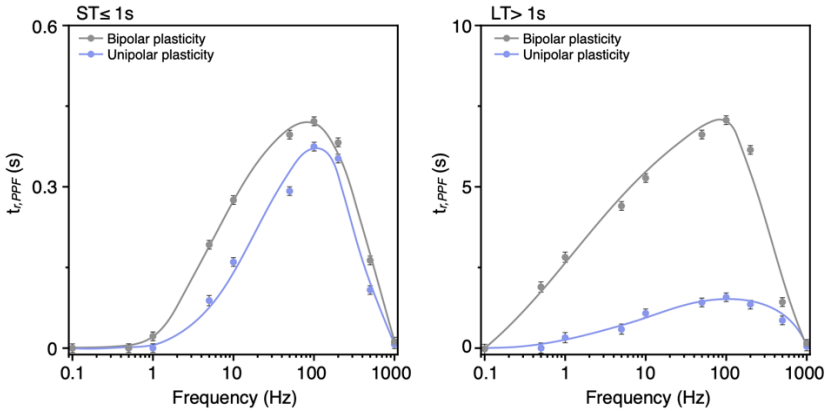

Supplementary Information Fig. 28: Frequency-dependent paired-pulse retention features of GIT$_{Ca/Al}$. Paired-pulse facilitation retention time ($t_{r,PPF}$) of the GIT$_{Ca/Al}$ with short- (ST)/long-term (LT) memory under varying pulse frequencies ranging from 0.1 Hz to 1000 Hz. Data are presented as mean ± s.d. from 5 independent measurements on the same sample (n = 5).

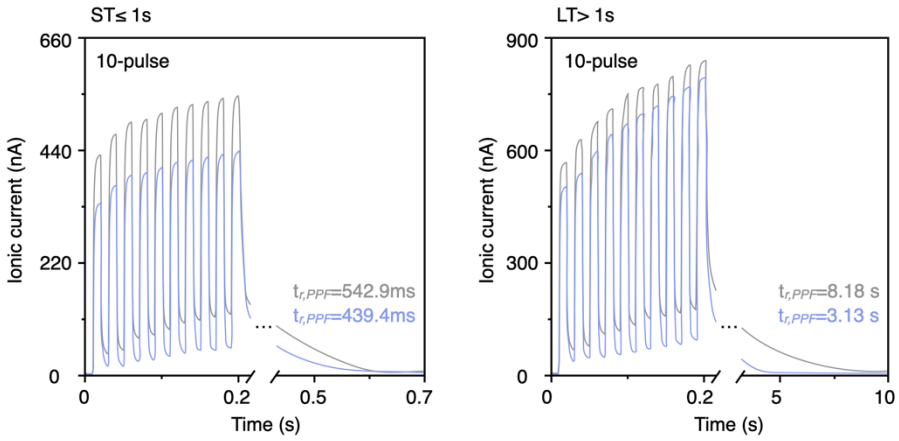

Supplementary Information Fig. 29: Ionic current response of $GIT_{Ca/Al}$ over 10 consecutive pulse sweeps. Ionic current of the $GIT_{Ca/Al}$ with short-/long-term memristive features under a 10-pulse voltage with a consistent pulse interval of 10 ms (square wave frequency of 100 Hz). (1^{st}: blue; 2^{nd}: gray)

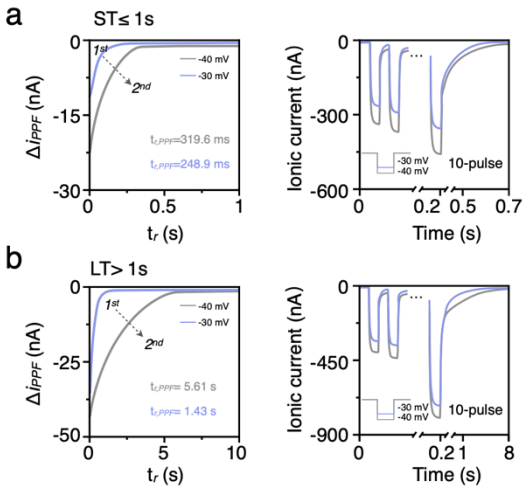

Supplementary Information Fig. 30: Paired-pulse facilitation behaviours of $GIT_{Ca/Al}$ under negative periodic voltage pulses. Paired-pulse facilitation postsynaptic current changes (Δi_{PPF}) and paired-pulse facilitation retention time ($t_{r,PPF}$)of the $GIT_{Ca/Al}$ with short-term (**a**) and long-term (**b**) memristive features. The corresponding ionic current of the $GIT_{Ca/Al}$ under periodic voltage pulses with a consistent pulse interval of 10 ms (square wave frequency of 100 Hz). Plateau voltage values are set to -30 mV (1^{st}) and -40 mV (2^{nd}).

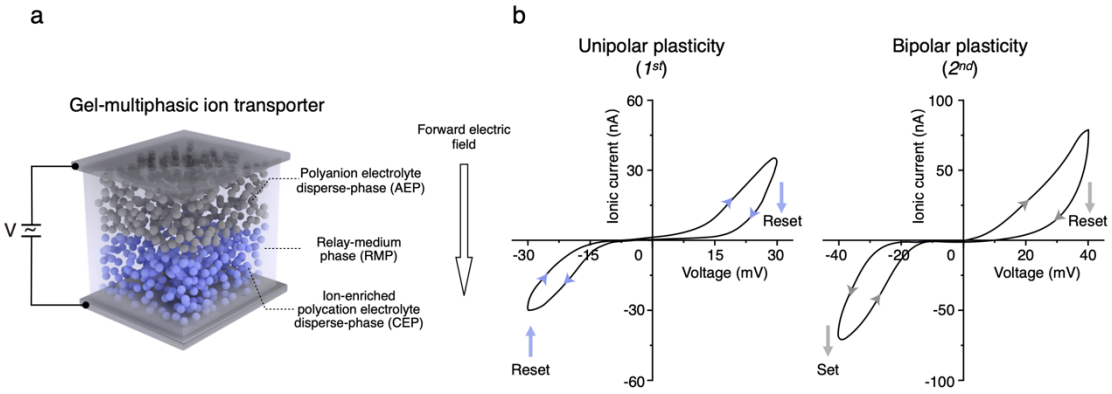

Supplementary Information Fig. 31: Dual-order plasticity of depression-featured $GIT_{Cl/ClO}$. a, Structural illustration of the depression-featured $GIT_{Cl/ClO}$, composed of a polyanion electrolyte disperse-phase (AEP), a relay medium-phase (RMP), and an ion-enriched polycation electrolyte disperse-phase (CEP). **b,** Distinct *I-V* characteristic curves of the $GIT_{Cl/ClO}$ exhibit dual-order (i.e., unipolar/ bipolar) plasticity features under periodic electric fields (1 mV/s).

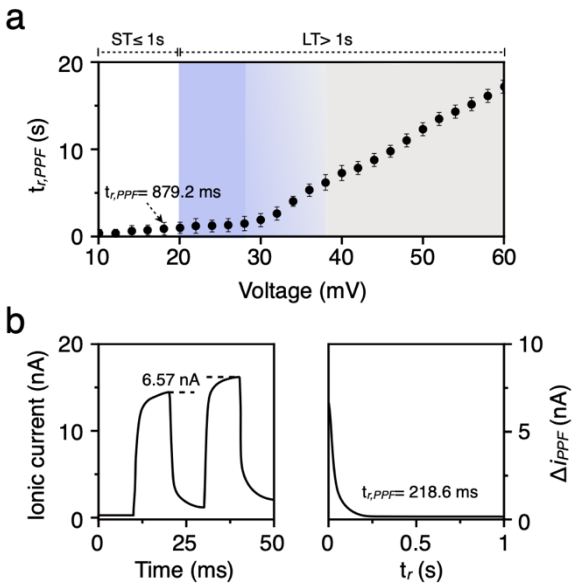

Supplementary Information Fig. 32: Spike-strength and memory timescale effects of the GIT systems. a, Paired-pulse facilitation retention time ($t_{r,PPF}$) of the $GIT_{Ca/Al}$ as a function of pulse amplitude (10-60 mV). When the pulse amplitude drops below approximately 18 mV, $t_{r,PPF}$ values fall below 1 s, indicating the transition from long-term (LT) to short-term (ST) memor y. The shaded regions indicate different plasticity modes: the blue region corresponds to the unipolar plasticity(1^{st}), the grey region corresponds to the bipolar plasticity (2^{nd}), and the blue-to-grey transition region represents the transition between unipolar- and bipolar plasticity. Data are presented as mean ± s.d. from 5 independent measurements on the same sample (n = 5). **b,** Ionic current responses of the $GIT_{Ca/Al}$ under 10 mV paired-pulse stimulation with a consistent pulse interval of 10 ms (square wave frequency of 100 Hz), and the corresponding paired-pulse facilitation postsynaptic current changes (Δi_{PPF}) of the $GIT_{Ca/Al}$.

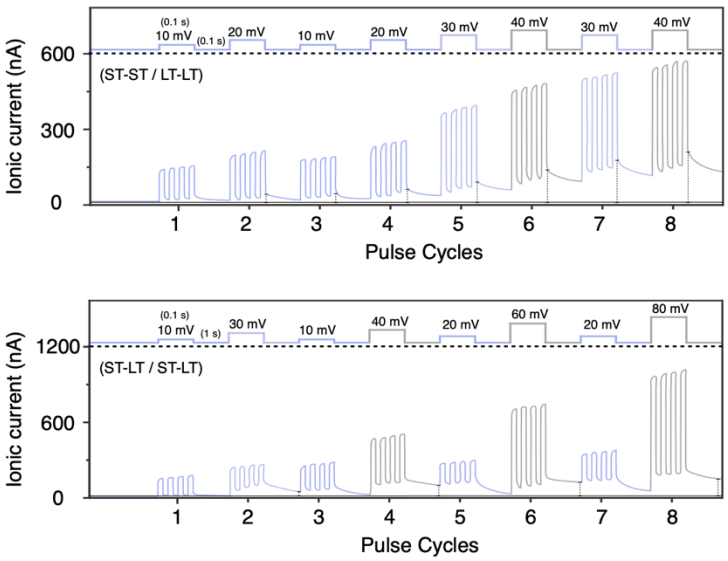

Supplementary Information Fig. 33: Temporally programming synaptic adaptability. Implementation of ion-based synaptic adaptability in the GIT system with long-term (LT) to short-term (ST) memory.

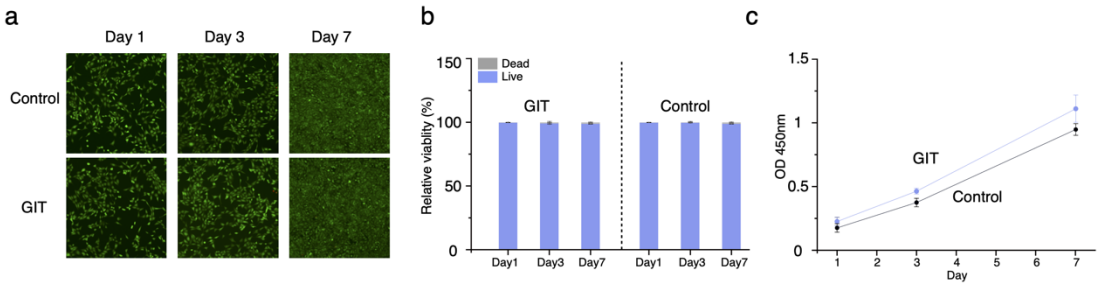

Supplementary Information Fig. 34: *In vitro* cytocompatibility of GITs. Live/dead fluorescence staining images show the changes in cell state on days 1, 3, and 7 of culture in the control and GIT-treated groups. Green fluorescence represents surviving cells. Both groups of cells exhibited good viability and continuous proliferation throughout the culture period, with cell density increasing significantly over time, forming a dense cell layer by day 7. Compared with the control group, no significant cytotoxicity or proliferation inhibition was observed in the GIT -treated group, indicating that the GIT system has good biocompatibility. Data are presented as mean ± s.d. from 3 independent measurements on the same sample (n = 3).

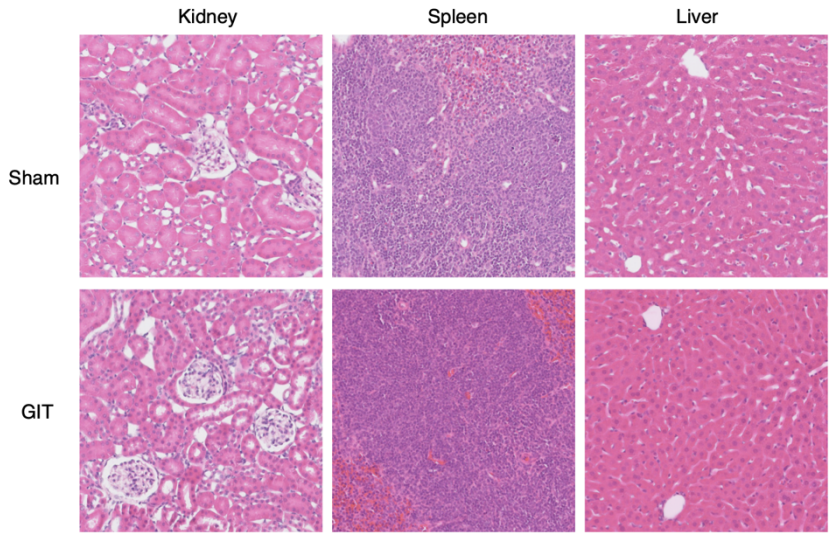

Supplementary Information Fig. 35: Histological evaluation after GIT implantation. Representative H&E staining images of major organs (kidney, spleen, and liver) from rats in the sham-operated control group (Sham) and the gel-implanted group (GIT). Scale bar:100μm. n=6.

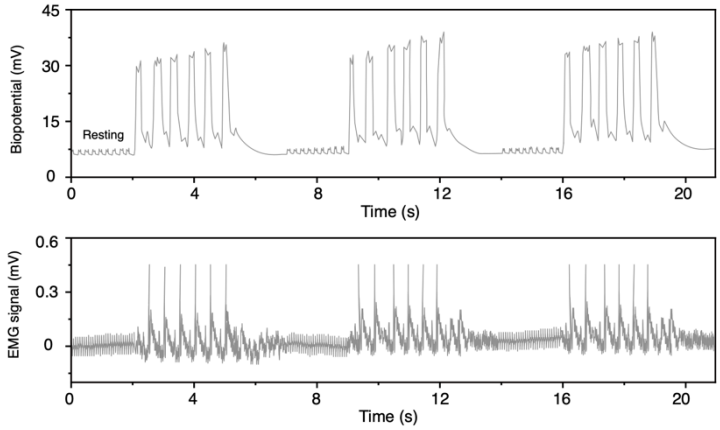

Supplementary Information Fig. 36: Original sciatic nerve and EMG signals. Original neural potential spike signals of the rat's sciatic nerve and corresponding EMG signals.

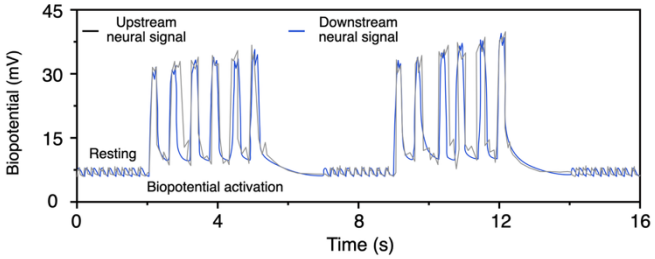

Supplementary Information Fig. 37: Downstream neural signal reconfiguration by GIT_{Ca}. By processing upstream neural potential spike signals from the proximal sciatic nerve, reconfigured downstream signals at the distal sciatic nerve by the GIT_{Ca} channel can closely match the original neural signals.

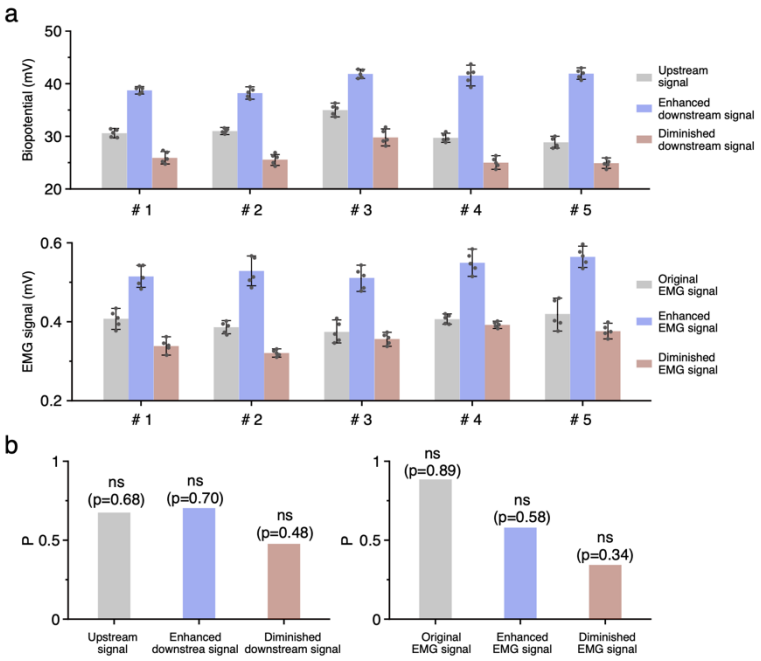

Supplementary Information Fig. 38: Reproducibility of neural and EMG signal modulation. a, Statistical analysis of the mean values and standard deviations of neural biopotential signals and electromyographic (EMG) signals recorded from five individual rats (#1-#5, n = 5). All peak signals of biopotential and EMG measurements were obtained from five rats, each tested across five period groups, with each group consisting of six consecutive stimulation pulses. Error bars indicate standard deviation (mean ± s.d.). **b,** Inter-animal statistical reproducibility analysis showing the calculated P-values (one-way ANOVA with post-hoc Tukey test) across all five rats' corresponding neural and EMG signal datasets. The P-values quantify the probability that the observed differences occurred by chance. Statistical notations: n.s., not significant ($p \geq 0.05$).

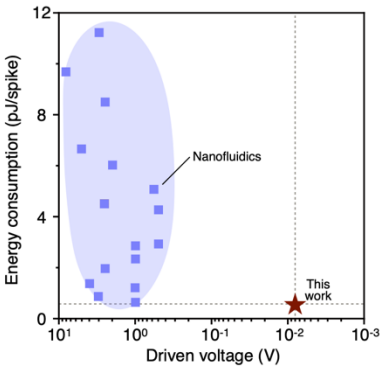

Supplementary Information Fig. 39: Energy consumption of ionic neuromorphic systems. The comparison of the lowest energy consumption in implementing ionic neuromorphics between the GIT and the nanofluidics.

Section 4: Supplementary Information Tables

Supplementary Information Table 1: Hydration free energies and diameters of the different ions.

Ion species	Bare diameter (Å)	Hydrated diameter (Å)	Hydration free energy (kJ/mol)
K^+	2.66	6.62	-295
Na^+	1.90	7.16	-365
Ca^{2+}	1.98	8.24	-1505
Al^{3+}	1.00	9.50	-4525

Supplementary Information Table 2: Comparison between GITs and other ion rectification systems.

Ion rectification systems	Rectification feature	Maximum rectification ratio	Driven-voltage (V)
Nanofluidic[7]	Unidirection	11620	5
Nanofluidic[8]	Unidirection	9130	1
Nanofluidic[7]	Unidirection	8735	1
Nanofluidic[9]	Unidirection	7213	2
Nanofluidic[10]	Unidirection	6973	4
Nanofluidic[11]	Unidirection	3283	7
Nanofluidic[12]	Unidirection	3061	2
Nanofluidic[13]	Unidirection	1603	1.2
Nanofluidic[14]	Unidirection	932	1
Nanofluidic[15]	Unidirection	693	1
Nanofluidic[16]	Unidirection	263	0.5
Nanofluidic[17]	Bidirection	255/-78	2
Nanofluidic[18]	Unidirection	218	1
Nanofluidic[19]	Unidirection	82	0.1
Nanofluidic[20]	Unidirection	48	0.5
Nanofluidic[21]	Unidirection	16	1
Microfluidic[22]	Unidirection	1559	4
Microfluidic[23]	Unidirection	631	2
Microfluidic[24]	Unidirection	392	2.5
Microfluidic[25]	Unidirection	237	5.5
Microfluidic[26]	Unidirection	159	5
Microfluidic[27]	Unidirection	104	2.5
Microfluidic[28]	Unidirection	61	6
Hydrogel[29]	Unidirection	97	1.5
Hydrogel[30]	Unidirection	60	2
Hydrogel[31]	Unidirection	41	1.8
Hydrogel[32]	Unidirection	33	1.2
Hydrogel[33]	Unidirection	28	2.5
Hydrogel[34]	Unidirection	18	1.9
Hydrogel[35]	Unidirection	14	1
Ionic liquid gel[36]	Unidirection	367	5
Ionic liquid gel[37]	Unidirection	291	8
Ionic liquid gel[38]	Unidirection	116	2
Ionic liquid gel[39]	Unidirection	83	3
Ionic liquid gel[40]	Unidirection	73	1
Conductive polymer[41]	Unidirection	550	0.35
Conductive polymer[42]	Unidirection	372	1.5
Conductive polymer[43]	Unidirection	192	1.5
Conductive polymer[44]	Unidirection	105	1
Conductive polymer[45]	Unidirection	65	3
Conductive polymer[46]	Unidirection	22	1.5
GIT system	Bidirection	1641/-1460	0.012-0.018

Supplementary Information Table 3: Comparison of ionic neuromorphic features between the GIT system and nanofluidic systems.

Device	The lowest energy consumption	Memory feature	Plasticity feature	Learning rule	Extra Gating field	Ion species
Nanofluidic[47]	1.98 pJ/spike	Short-term	Single-order	No	Voltage gating	1
Nanofluidic[48]	6.71 pJ/spike	Long-term Short-term	Single-order	No	Voltage gating	1
Nanofluidic[49]	2.75 pJ/spike	Long-term Short-term	Single-order	No	Voltage gating	1
Nanofluidic[50]	9.73 pJ/spike	Long-term Short-term	Single-order	No	Voltage gating	1
Nanofluidic[51]	/	Long-term Short-term	Single-order	Hebbian/ Anti-Hebbian learning rule	Voltage gating	1
Nanofluidic[52]	2.45 pJ/spike	Short-term	Single-order	No	Voltage gating	1
Nanofluidic[53]	0.66 pJ/spike	Short-term	Single-order	No	Voltage gating	4
Nanofluidic[54]	3.51 pJ/spike	Long-term Short-term	Single-order	No	Voltage gating	1
Nanofluidic[55]	4.32 pJ/spike	Long-term Short-term	Single-order	No	Voltage gating	1
Nanofluidic[56]	2.99 pJ/spike	Long-term Short-term	Single-order	No	Voltage gating	1
Nanofluidic[57]	5.13 pJ/spike	Long-term Short-term	Single-order	No	Voltage gating	1
Nanofluidic[58]	11.23 pJ/spike	Short-term	Single-order	No	Voltage gating	1
Nanofluidic[59]	8.51 pJ/spike	Long-term Short-term	Single-order	No	Voltage gating	1
Nanofluidic[60]	0.89 pJ/spike	Long-term Short-term	Single-order	No	Voltage gating	1
Nanofluidic[61]	1.39 pJ/spike	Short-term	Single-order	No	Voltage gating	1
Nanofluidic[62]	6.04 pJ/spike	Short-term	Single-order	No	Voltage gating	1
Nanofluidic[63]	3.86 pJ/spike	Long-term Short-term	Single-order	No	Voltage gating	1
GIT system	0.61 pJ/spike	Long-term Short-term	Dual-order	Hebbian/ Anti-Hebbian/ BCM learning rule	Non-gating	≥16

Supplementary Table 4: Corresponding explanation of the professional terminologies used in this work.

Professional terminologies	Corresponding explanation
Ionic cross-interface transfer energy barriers	The related energy consumption of ion cross-interface transport from the polyelectrolyte disperse-phase to the low-conductive relay-medium phase to the next polyelectrolyte disperse-phase.
ionic nonlinear transmission	Under the applied electric field, the current-voltage relationship of ion transport no longer follows simple Ohm's law (i.e., a linear relationship) but instead exhibits a nonlinear response, representing a non-Ohmic phenomenon.
Asymmetric central interfacial charge accumulation	Owing to the distinct transmission efficiencies between cations and anions across cascaded sub-heterointerfaces, coupled with electrostatic partition inversion at the center-heterointerface, both cations and anions undergo interface retardation effect at the center-heterointerface, leading to asymmetric charge accumulation.
Ionic bipolarity rectification	Compared to the unipolarity rectification with the fixed unidirectional conduction transition (i.e., on-to-off, forward electrical field; off-to-on, reverse electrical field), the bipolarity rectification represents a bipolar conduction transition from high to low conductance under both directional electrical field (i.e., on-to-off, forward and reverse electrical field).
Spike-strength/timing dependent plasticity	The postsynaptic current responds dynamically strengthened or weakened (modulated) according to the amplitude and relative timing of spikes.
Dual-order (i.e., unipolar and bipolar) plasticity	Dual-order plasticity denotes the distinct conductance modulation process in the GIT system for different *I-V* hysteresis behaviors, where the system exhibits either dual-set transitions (unipolar) or set/reset transitions (bipolar). Under periodic *I-V* scanning, unipolar plasticity represents an identical conductance transition trend across different *I-V* quadrants (e.g., LICS to HICS (set)). Bipolar plasticity represents opposite conductance transition trends across different *I-V* quadrants (e.g., LICS to HICS (set) and HICS to LICS (reset)).
Short-term (ST) and long-term (LT) behaviors	The retention time of the postsynaptic current, which corresponds to the decay time of the peak postsynaptic current to its baseline after paired stimulation, with ST defined as ≤ 1 s and LT as > 1 s.
Postsynaptic ionic current change (Δi)	$\Delta i = i_2 - i_1$, where i_1 and i_2 represent the postsynaptic ionic currents generated by the first and second voltage pulses, respectively.
Paired-pulse facilitation/depression retention times ($t_{r,PPF}$ and $t_{r,PPD}$)	The retention time of the facilitation or depression-type postsynaptic current after paired stimulation.
Plasticity factor (k)	The slope of t_r with respect to the amplitude of the spike voltage.
Synaptic connection strength (ΔG)	$\Delta G = (G_F - G_O)/ G_O$, where G_O and G_F represent the conductance values measured under the original and final spikes.

References

1. Robertson, M. J. et al. Improved peptide and protein torsional energetics with the OPLS-AA force field. *J. Chem. Theory. Comput.* **11**, 3499–3509 (2015).

2. Jorgensen, W. L. et al. Comparison of simple potential functions for simulating liquid water. *J. Chem. Phys.* **79**, 926–935 (1983).

3. Faro, T. M. C. et al. A Lennard-Jones plus Coulomb potential for Al^{3+} ions in aqueous solutions. *J. Chem. Phys.* **132**, 114509 (2010).

4. Ryckaert, J.-P. et al. Numerical integration of the cartesian equations of motion of a system with constraints: molecular dynamics of n-alkanes. *J. Comput. Phys.* **23**, 327–341 (1977).

5. Plimpton, S. Fast Parallel algorithms for short-range molecular dynamics. *J. Comput. Phys.* **117**, 1–19 (1995).

6. Hub, J. S. et al. g_wham—a free weighted histogram analysis implementation including robust error and autocorrelation estimates. *J. Chem. Theory Comput.* **6**, 3713–3720 (2010).

7. Chen, L. et al. Unidirectional ion transport in nanoporous carbon membranes with a hierarchical pore architecture. *Nat. Commun*. **12**, 4650 (2021).

8. Wang, X. et al. High rectification ratios of Fe–porphyrin molecules on Au facets. *Mater. Chem. Phys.* **136**, 190–195 (2012).

9. Wang, Y. et al. “Ion pool” structural ion storage device: a new strategy to collect ions by nanoconfinement effects. *Small* **17**, 2102880 (2021).

10. Wei, Y. et al. GaN nano air channel diodes: enabling high rectification ratio and neutron robust radiation operation. *Adv. Sci*. **11**, 2310300 (2024).

11. Nandigana, V. V. R. et al. Asymmetric-fluidic-reservoirs induced high rectification nanofluidic diode. *Sci. Rep.* **8**, 13941 (2018).

12. Kim, J. et al. Multi-layered bipolar ionic diode working in broad range ion concentration. *Micromachines* **14**, 1311 (2023).

13. Ashery, A. et al. Investigation of electrical and dielectric properties of epitaxially grown Au/n-GaAs/p-Si/Al heterojunction. *Opt Quant Electron* **52**, 490 (2020).

14. Li, Z. et al. Bioinspired multivalent ion responsive nanopore with ultrahigh ion current rectification. *J. Phys. Chem. C.* **123**, 13687–13692 (2019).

15. Sapkota, K. R. et al. Ultralow Voltage GaN Vacuum Nanodiodes in Air. *Nano Lett.* **21**, 1928–1934 (2021).

16. Liu, M. et al. Excellent field emission properties of VO_2(A) nanogap emitters in air. *Appl. Phys. Lett.* **112**, 93104 (2018).

17. Lu, J. et al. Ultrafast rectifying counter-directional transport of proton and metal ions in metal-organic framework-based nanochannels. *Sci. Adv.* **8**, eabl5070 (2022).

18. Liu, F. et al. In situ synthesis of a MOFs/PAA hybrid with ultrahigh ionic current rectification. *Nanoscale* **12**, 11899–11907 (2020).

19. Wang, G. et al. Introduction of interfacial charges to black phosphorus for a family of planar devices. *Nano Lett.* **16**, 6870–6878 (2016).

20. Chang, W.-T. et al. Metal-based asymmetric field emission diodes operated in the air. *Microelectron. Eng.* **232**, 111418 (2020).

21. Xin, W. et al. Biomimetic KcsA channels with ultra-selective K^+ transport for monovalent ion sieving. *Nat. Commun.* **13**, 1701 (2022).

22. He, X. et al. Micrometer-scale ion current rectification at polyelectrolyte brush-modified micropipets. *J. Am. Chem. Soc.* **139**, 1396–1399 (2017).

23. Yao, Z. et al. Simultaneous implementation of resistive switching and rectifying effects in a metal-organic framework with switched hydrogen bond pathway. *Sci. Adv.* **5**, eaaw4515 (2025).

24. Zhang, Z. et al. Engineered asymmetric heterogeneous membrane: a concentration-gradient-driven energy harvesting device. *J. Am. Chem. Soc.* **137**, 14765–14772 (2015).

25. Xia, X.H. Marked ion current rectification in microchannels. *Sci. China Chem.* **60**, 685–686 (2017).

26. Liu, W. et al. A universal design of field-effect-tunable microfluidic ion diode based on a gating cation-exchange nanoporous membrane. *Phys. Fluids*. **29**, 112001 (2017).

27. Miller, S. A. et al. Ionic current rectification at a nanofluidic/microfluidic interface with an asymmetric microfluidic system. *Lab Chip.* **8**, 1729‑1732 (2008).

28. Wang, H. et al. Controlling the ionic current rectification factor of a nanofluidic/microfluidic interface with symmetric nanocapillary interconnects. *Anal. Chem.* **87**, 3598–3605 (2015).

29. Huo, R. et al. Tough transient ionic junctions printed with ionic microgels. *Adv. Funct. Mater.* **33**, 2213677 (2023).

30. Tabanli, S. et al. Polyacrylamide hydrogel as an electrolyte for oxidation-based organic rectifiers. *Polym. Eng. Sci.* **55**, 406-413 (2015).

31. Nyamayaro, K. et al. The rectification mechanism in polyelectrolyte gel diodes. *Phys. Fluids.* **33**, 032010 (2021).

32. Nyamayaro, K. et al. Toward biodegradable electronics: ionic diodes based on a cellulose nanocrystal-agarose hydrogel. *ACS Appl. Mater. Interfaces.* **12**, 52182–52191 (2020).

33. Jiang, F. et al. Ion rectification based on gel polymer electrolyte ionic diode. *Nat. Commun.* **13**, 6669 (2022).

34. Cayre, O. J. et al. Polyelectrolyte diode: nonlinear current response of a junction between aqueous ionic gels. *J. Am. Chem. Soc.* **129**, 10801–10806 (2007).

35. Huang, K. T. et al. Zwitterionic gradient double-network hydrogel membranes with superior biofouling resistance for sustainable osmotic energy harvesting. *Adv. Funct. Mater.* **33**, 2211316 (2023).

36. Xing, Y. et al. Integrated opposite charge grafting induced ionic-junction fiber. *Nat. Commun.* **14**, 2355 (2023).

37 Luo, J. et al. Poly(ionic liquid) additive: aqueous electrolyte engineering for ion rectifying and calendar corrosion relieving. *Chem. Eng. J.* **470**, 144152 (2023).

38. Li, D. et al. Reversed rectification of ionic liquid/water mixtures in conical nanochannels, *Nanotechnol. Precis. Eng.* **8**, 013009 (2025).

39. So, J.-H. et al. Ionic current rectification in soft-matter diodes with liquid-metal electrodes. *Adv. Funct. Mater.* **22**, 625‑631 (2012).

40. Lim, S.-M. et al. Ion-to-ion amplification through an open-junction ionic diode. *Proc. Natl. Acad. Sci.* **116**, 13807‑13815 (2019).

41. Kim, H. J. et al. Ionoelastomer junctions between polymer networks of fixed anions and cations. *Science* **367**, 773‑776 (2020)

42. Gao, Z. et al. Hybrid electromagnetic and moisture energy harvesting enabled by ionic diode films. *Nat. Commun.* **16**, 312 (2025).

43. Pérez-Mitta, G. et al. An all-plastic field-effect nanofluidic diode gated by a conducting polymer layer. *Adv. Mater.* **29**, 1700972 (2017).

44. Zhang, Q. et al. Redox switch of ionic transport in conductive polypyrrole-engineered unipolar nanofluidic diodes. *Nano Res.* **10**, 3715‑3725 (2017).

45. Hao, J. et al. A euryhaline-fish-inspired salinity self-adaptive nanofluidic diode leads to high-performance blue energy harvesters. *Adv. Mater.* **34**, 2203109 (2022).

46. Pérez-Mitta, G. et al. Nanofluidic diodes with dynamic rectification properties stemming from reversible electrochemical conversions in conducting polymers. *J. Am. Chem. Soc.* **137**, 15382‑15385 (2015).

47. Yang, R. et al. Negative differential resistance in conical nanopore iontronic memristors. *J. Am. Chem. Soc.* **146**, 13183‑13190 (2024).

48. Ling, Y. et al. Single-pore nanofluidic logic memristor with reconfigurable synaptic functions and designable combinations. *J. Am. Chem. Soc.* **146**, 14558‑14565 (2024).

49. Mei, T. et al. Bio-inspired two-dimensional nanofluidic ionic transistor for neuromorphic signal processing. *Angew. Chem Int. Ed.* **63**, e202401477 (2024).

50. Wang, L. et al. Ionic potential relaxation effect in a hydrogel enabling synapse-like information processing. *ACS Nano* **18**, 29704−29714 (2024).

51. Robin, P. et al. Long-term memory and synapse-like dynamics in two-dimensional nanofluidic channels. *Science* **379**, 161–167 (2023).

52. Dai, J. et al. Artificial nerve for neuromodulation based on structured piezoionic hydrogel. *Device* **2**, 100436 (2024).

53. Xiong, T. et al. Neuromorphic functions with a polyelectrolyte-confined fluidic memristor. *Science* **379**, 156–161 (2023).

54. Niu, Y. et al. Soft memristor at a microbubble interface. *Nano Lett.* **24**, 10475‑10481 (2024).

55. Yu, S. Y. et al. Metal-organic framework nanofluidic synapse. *J. Am. Chem. Soc.* **146**, 27022‑27029 (2024).

56. Li, P. et al. Artificial funnel nanochannel device emulates synaptic behavior. *Nano Lett.* **24**, 6192‑6200 (2024).

57. Hana, S. H. et al. Iontronic analog of synaptic plasticity: hydrogel-based ionic diode with chemical precipitation and dissolution. *Proc. Natl. Acad. Sci.* **120**, e2211442120 (2023).

58. Zhang, Z. et al. Geometrically scalable iontronic memristors: employing bipolar polyelectrolyte gels for neuromorphic systems. *ACS Nano* **18**, 15025‑15034 (2024).

59. Wang, J. et al. Optically modulated nanofluidic ionic transistor for neuromorphic functions. *Angew. Chem Int. Ed.* 202418949 (2024).

60. Xiao, Y. et al. Neural functions enabled by a polarity-switchable nanofluidic memristor. *Nano Lett.* **24**, 12515−12521 (2024).

61. Zhou, X. et al. Nanofluidic memristor based on the elastic deformation of nanopores with nanoparticle adsorption. *Natl. Sci. Rev.* **11**, nwad216 (2024).

62. Wang, W. et al. Memristive characteristics in an asymmetrically charged nanochannel. *J. Phys. Chem. Lett.* **15**, 6852‑6858 (2024).

63. Ma, Y. et al. Reconfigurable neuromorphic computing by a microdroplet. *Cell Reports Phys. Sci.* **5**, 102202 (2024).